Main title: Minor spliceosome inactivation causes microcephaly due to cell cycle defects and death of self-amplifying radial glial cells.

Marybeth Baumgartner[1,2,#], Anouk M. Olthof[1,#], Gabriela S. Aquino[1], Katery C. Hyatt[1], Christopher Lemoine[1,3], Kyle Drake[1], Nikita Sturrock[1,4], Nhut Nguyen[1], Sahar al Seesi[5], Rahul N. Kanadia[1,6,*]

[1]Physiology and Neurobiology Department, University of Connecticut, Storrs, CT 06269, USA [2]Connecticut Institute for the Brain and Cognitive Sciences, University of Connecticut, Storrs, CT 06269, USA [3]College of Medicine, University of Illinois, Chicago, IL 60612, USA [4]Harvard Medical School, Boston, MA 02115, USA [5]Computer Science Engineering Department, University of Connecticut, Storrs, CT 06269, USA [6]Institute of Systems Genomics, University of Connecticut, Storrs, CT 06269, USA

*Corresponding author #Contributed equally

Correspondence to Dr. Rahul N. Kanadia can be sent by mail, to 75 N Eagleville Rd, Storrs, CT 06269; by phone, at (860)-486-0286; or by e-mail, at rahul.kanadia@uconn.edu.

Keywords. Cortical development; microcephaly; radial glial cells; minor spliceosome; U11 snRNA; cell cycle

Summary Statement. Here we report the first mammalian model to investigate the role of the minor spliceosome in cortical development and microcephaly.

Abstract. Mutation in minor spliceosome components is linked to the developmental disorder microcephalic osteodysplastic primordial dwarfism type 1 (MOPD1). Here we inactivated the minor spliceosome in the developing mouse cortex (pallium) by ablating *Rnu11*, which encodes the crucial minor spliceosome snRNA U11. *Rnu11* conditional knockout mice were born with microcephaly, which was caused by the death of self-amplifying radial glial cells (RGCs), while intermediate progenitor cells and neurons were produced. RNAseq suggested that this cell death was mediated by upregulation of p53 and DNA damage, which were both observed specifically in U11-null RGCs. Moreover, U11 loss caused elevated minor intron retention in genes regulating cell cycle, which was consistent with fewer RGCs in S-phase and cytokinesis, alongside prolonged metaphase in RGCs. In all, we found that self-amplifying RGCs are the cell type most sensitive to loss of minor splicing. Together, these findings provide a potential explanation of how disruption of minor splicing might cause microcephaly in MOPD1.

List of abbreviations used. MOPD1=microcephalic osteodysplastic primordial dwarfism type 1; snRNA=small nuclear RNA; cKO=conditional knockout; NPC=neural progenitor cell; RGC=radial glial cell; IPC=intermediate progenitor cell; MIG=minor intron-containing gene

Introduction. RNA splicing, the removal of non-coding introns from pre-mRNA transcripts, is an essential step in eukaryotic gene expression. This process is performed by one of two distinct spliceosomes, the major or the minor type (Patel and Steitz, 2003). The minor spliceosome contains four unique snRNAs (U11, U12, U4atac, and U6atac) and the U5 snRNA, which it shares with the major spliceosome (Tarn and Steitz, 1996b; Tarn and Steitz, 1996a). Less than 0.5% of introns require the minor spliceosome for their removal; hence, they are called minor introns (Alioto, 2007). The importance of minor intron splicing in development is underscored by the discoveries that hypomorphic mutation in the U4atac snRNA causes the developmental disorders microcephalic osteodysplastic primordial dwarfism type 1 (MOPD1), Roifman syndrome, and Lowry Wood syndrome (He et al., 2011; Merico et al., 2015; Farach et al., 2018). All three disorders, despite being caused by systemic loss of minor splicing, are characterized by microcephaly and dwarfism, which suggests a tissue-specific requirement for the minor spliceosome in development (He et al., 2011; Merico et al., 2015; Farach et al., 2018). Therefore, to understand the mechanism of disease pathogenesis underlying microcephaly in these syndromes, it is important to study the regulation of minor intron-containing genes (MIGs) in cortical development.

Proper cortical development requires a balance between amplification of the neural progenitor cells (NPCs) and neurogenesis. Overproduction of neurons at the expense of self-amplifying NPC divisions can deplete the NPC pool early in cortical development, resulting in microcephaly (Homem et al., 2015). The decision of an NPC to produce a neuron is regulated by cell cycle length, particularly the length of G1 and mitosis (Calegari and Huttner, 2003; Lange et al., 2009; Pilaz et al., 2009; Pilaz et al., 2016). Cell cycle defects that lengthen these phases would result in increased neuron production. Additionally, the presence of two different NPC types, radial glial cells (RGCs) and intermediate progenitor cells (IPCs), can regulate neurogenesis. RGCs can undergo

symmetric proliferative divisions, which produce two RGCs, or asymmetric differentiative divisions, to produce one RGC and either one IPC or one neuron. In contrast, most IPCs undergo symmetric neurogenic divisions, to produce two neurons (Gotz and Huttner, 2005). A small fraction undergoes symmetric proliferative division, producing two IPCs, prior to symmetric neurogenic division (Noctor et al., 2004). Ultimately, RGCs are required to maintain the NPC population, while IPCs primarily contribute to neuron production (Kowalczyk et al., 2009). In short, microcephaly can be caused by (1) death of the NPC or neuronal populations; (2) increased neuron production, resulting in depletion of the NPC pool; and/or (3) decreased IPC production, resulting in fewer neurons. It is unclear how these processes are affected by loss of minor splicing in MOPD1, Roifman syndrome, and Lowry Wood syndrome. Here, we report the role of minor splicing in mammalian cortical development. For this, we leveraged a novel conditional knockout (cKO) mouse for the gene encoding the U11 snRNA, a crucial component of the minor spliceosome (Kolossova and Padgett, 1997).

Results

Constitutive loss of U11 is embryonically lethal. We generated the *Rnu11* cKO mouse by engineering loxP sites 1090 bp upstream and 1159 bp downstream of the *Rnu11* gene (Fig. 1A and S1). Successful targeting of the loxP sites was confirmed by long-range nested PCR in targeted embryonic stem cells (Fig. S1B-C) and further validated by the loss of the wild-type (WT) allele in *Rnu11$^{Flx/Flx}$* mice (Fig. 1A). *EIIa*-Cre-mediated germline recombination generated *Rnu11$^{WT/KO}$* mice, which showed the presence of the KO allele that was absent in *Rnu11$^{WT/WT}$* genomic DNA (Fig. 1A). Quantitative PCR (qPCR) for the WT allele showed 50% reduction in *Rnu11$^{WT/KO}$* mice compared to *Rnu11$^{WT/WT}$* mice (Fig. 1B). Intercrossing *Rnu11$^{WT/KO}$* mice did not yield *Rnu11$^{KO/KO}$* mice (Fig. 1C), indicating embryonic lethality.

Ablation of U11 in the pallium causes microcephaly. We employed *Emx1*-Cre mice to specifically ablate *Rnu11* in the pallium (Gorski et al., 2002). *Emx1*-Cre expression begins at E9.5 in the neuroepithelium of the pallium, prior to the production of RGCs, IPCs, or neurons at E10-E11 (Gorski et al., 2002). Ablation of U11 in the pallium resulted in profound microcephaly at birth in *Rnu11$^{Flx/Flx}$*::*Emx1*-Cre$^{+/-}$ mutant mice, due to collapse of the cortex and absence of the hippocampus (Fig. 1D). To understand how this microcephaly precipitated, we sought to determine the kinetics of U11 snRNA loss after *Emx1*-Cre-mediated *Rnu11* ablation. *In situ* hybridization (ISH) for U11 snRNA revealed a reduction in U11 signal (purple) in the E10 mutant pallium, relative to the control (*Rnu11$^{WT/Flx}$*::*Emx1*-Cre$^{+/-}$) (Fig. 1E). This U11-null domain was expanded in the E11 mutant pallium, and by E12, the majority of cells in the *Emx1*-Cre domain lacked U11 expression (Fig. 1F&G). We observed scattered U11$^+$ cells at this point (Fig. 1G), which may represent either inefficient *Emx1*-Cre recombination or migrating interneurons produced in the ventral telencephalon, where *Emx1*-Cre is not active (Gorski et al., 2002; Bartolini et al., 2013). There was no observable morphological difference between mutant and littermate control pallia at E10, E11, and E12 (Fig. 1E-G). At E13, we observed persistence of the U11-null domain alongside collapse of

the lateral ventricle in the mutant telencephalon, without a significant change in pallial thickness (Fig. 1H&J). At E14, the thickness of the mutant pallium was significantly reduced relative to the control (Fig. 1I-J).

Cell death contributes to microcephaly in the U11 cKO mice. We first performed fluorescent ISH (FISH) for U11 to identify the U11-null domain, followed by terminal dUTP nick-end labeling (TUNEL) to detect apoptotic cells. Results showed sporadic loss of U11 snRNA in the E11 mutant pallium without a significant increase in TUNEL$^+$ cells (Fig. 2A). Onset of cell death was observed at E12, with a statistically significant increase in TUNEL$^+$ cells in the mutant compared to littermate controls (Fig. 2B), which continued at E13 and E14 (Fig. 2C-D). Since TUNEL marks cells in late stages of apoptosis, we sought to verify the timing of cell death in the mutant pallium using a marker of early apoptosis (Kyrylkova et al., 2012). For this, we employed immunofluorescence (IF) for cleaved caspase 3 (CC3) (Faleiro et al., 1997) at E11 and E12, which confirmed that the onset of cell death was occurring at E12 (Fig. 2E-F).

Microcephaly is predominantly caused by loss of NPCs. To identify the cell type being lost in the mutant pallium, we investigated the numbers of proliferating NPCs (Ki67$^+$) versus neurons (NeuN$^+$) by IF (Wolf et al., 1996; Scholzen and Gerdes, 2000). We found no change in the number of proliferating NPCs in the E12 mutant pallium compared to the control (Fig. 3A&D). However, at E13 and E14, the number of Ki67$^+$ NPCs was significantly reduced in the mutant pallium compared to the control (Fig. 3B-D). Unlike NPCs, we did not observe a significant difference in the number of neurons between the control and mutant at E12 or E13 (Fig. 3A-B&D). To confirm that the neurons present in the E12 and E13 mutant pallium were in fact U11-null, we performed U11 FISH in conjunction with IF for Ki67 and NeuN, which showed the presence of both U11-null NPCs and U11-null neurons (Fig. S2A). Finally, at E14, there were significantly fewer neurons in the mutant compared to the control, which was consistent with the depletion of the NPC population at E13 (Fig. 3B-D). To further investigate whether neurons were dying in the U11-null pallium, we employed IF for Tuj1, which marks both immature and mature neurons (Zhang and Jiao, 2015), and CC3, and quantified the percentage of CC3$^+$ dying cells that were Tuj1$^+$ neurons. In the E12 mutant pallium, the vast majority (93.4±2.1%) of the CC3$^+$ cells were pyknotic, indicative of late-stage apoptotic cells (Fig. S2C). By E13, virtually all CC3$^+$ cells were pyknotic (data not shown). Since pyknotic cells in the late stages of apoptosis are unlikely to retain Tuj1 expression, we only considered non-pyknotic CC3$^+$ cells for the analysis. This quantification revealed that 4.44±2.42% of non-pyknotic CC3$^+$ cells in the E12 mutant pallium were Tuj1$^+$ neurons, which was not significantly higher than that observed in the control (0%; Fig. S2C). Together, these data suggested that most of the dying cells were likely the U11-null NPCs, not the U11-null neurons.

Self-amplifying RGCs require the minor spliceosome for survival. We next sought to identify the type of NPC being lost in the U11-null pallium. Using the nuclear RGC marker Pax6, we did not observe a significant difference in the number of RGCs between the control and mutant at E12 (Fig. 3E&H) (Gotz et al., 1998). At E13, there was a significant reduction in the number of RGCs with nuclear Pax6 signal in the mutant compared to the control (Fig. 3F&H). However, widespread cytoplasmic Pax6 expression, which was rarely seen in control sections, was observed in the mutant (Fig. 3F). This cytoplasmic staining was primarily observed around condensed nuclei, suggesting that the cytoplasmic Pax6 expression was occurring in dying cells. This was confirmed by colocalization of the cytoplasmic Pax6 expression with CC3 (Fig. S2B-B'''). Therefore, only cells with nuclear Pax6 expression were quantified. At E14, there were few RGCs in the mutant, which was consistent with the small number of Ki67$^+$ cells at this time-point (Fig. 3D&G-H). Next, we investigated the number of IPCs in the U11-null pallium using the marker Tbr2 (Englund et al., 2005), which revealed no significant difference in the E12 mutant compared to the control (Fig. 3I&L). At E13, we observed a significant reduction in the IPC population in the mutant relative to the control (Fig. 3J&L), which continued at E14 (Fig. 3K-L).

Both the RGC and IPC populations were significantly reduced in the mutant pallium at E13, but not at E12, relative to the control (Fig. 3D&H). However, the trends of RGC and IPC loss across mutant pallium development were not similar: While there was a significant decline in the number of RGCs in the E13 mutant pallium compared to the E12 mutant pallium, there was no significant change in the number of IPCs between these time-points in the mutant (Fig. S2D-E). A significant decline in IPC number was only observed between E13 and E14 mutant pallium (Fig. S2E). Therefore, the decline in RGC number occurred earlier in the mutant pallium than the decline in IPCs, suggesting that IPCs were being produced in the U11-null pallium.

The observation that the E13 control and mutant pallia both contained similar numbers of neurons suggested that neuron production was also occurring in the E12 mutant pallium (Fig. 3B&D). To study neuron production in the mutant pallium, we pulsed pregnant dames carrying E12 embryos with the thymidine analog 5-bromo-2'-deoxyruidine (BrdU), to mark S-phase NPCs, followed by harvest at E13 (Takahashi et al., 1995). After removing pyknotic BrdU$^+$ cells, quantification showed that a significant decrease in NeuN$^+$/BrdU$^+$ cells as a percentage of all NeuN$^+$ cells in the E13 mutant pallium compared to the control. In contrast, there was no significant difference in the percentage of non-pyknotic BrdU$^+$ cells that were NeuN$^+$ between the E13 control (15.7±2.17%) and mutant (15.5±3.5%; Fig. S2F) pallium. The presence of BrdU$^+$ neurons in the mutant indicated that U11-null NPCs produced neurons between E12 and E13. Together, these findings suggested that the majority of cells dying between E12 and E13 were self-amplifying RGCs.

DNA damage and p53 upregulation occur in U11-null RGCs. To understand the molecular defects underlying the loss of self-amplifying RGCs, we performed RNAseq on control (*N*=5) and mutant (*N*=5) pallia from E12 embryos (Fig. 4A inset). At this time-point, U11 loss occurs throughout the entire *Emx1*-Cre domain without major histological changes, such as shifts in NPC number (Fig. 1G and 3D). Confirmation of the pallial dissection was reflected by the expression of *Emx1* in the control (19.1 fragments per kilobase per million mapped reads [FPKM]) and mutant (20.3 FPKM). Expression of *Dbx1*, which marks the pallial-subpallial boundary, and *Lhx6*, which is expressed in the medial ganglionic eminence (Grant et al., 2012), were expressed below 1 FPKM in both the control and mutant samples (Table S1). Together, these results confirm the integrity of our dissection. Expression of *Rnu11* was reduced by 2.95 fold in the mutant compared to the control, which was further confirmed by quantitative reverse transcriptase-PCR (qRT-PCR) (Fig. 4B, Table S1). The incomplete loss of U11 expression in the mutant likely reflects (1) contamination of non-*Emx1*-lineage cells of the meninges and blood vessels (Fig. 1G) (Siegenthaler and Pleasure, 2011); (2) contamination from non-*Emx1*-lineage cells migrating into the pallium (Fig. 1G) (Bartolini et al., 2013); and/or (3) incomplete recombination by *Emx1*-Cre. Regardless, the mutant samples showed a clear reduction in U11 expression compared to the control, which was in agreement with the ISH analysis (Fig. 1G). Next, we interrogated the expression of all protein-coding genes with ≥1 FPKM in the control or mutant. Overall, there was an increase in the number of genes upregulated (74; ≥2-fold change [FC], *P*≤0.01) relative to those downregulated (11; ≥2-FC, *P*≤0.01) in the mutant (Fig. 4A, Table S1). DAVID analysis (Huang da et al., 2009) performed on the downregulated protein-coding genes revealed no significant enrichments for GO-terms by Benjamini score. However, the upregulated protein-coding genes significantly enriched for the GO-term "intrinsic apoptotic signaling pathway in response to DNA damage by p53 class mediator" (Table S2), implicating this pathway in the cell death observed at this time-point (Fig. 2).

To test whether DNA damage and p53 activation were occurring in the E12 mutant, we employed IF with the DNA damage marker γH2AX (Sharma et al., 2012), along with antibody against p53. We observed that the majority of γH2AX$^+$ cells were pyknotic (54.1±3.5%), suggesting that they were dying cells (Fig. 4D). To verify this, we employed the early-apoptotic marker CC3, which revealed that 93.2±3.5% of γH2AX$^+$ cells were CC3$^+$ (Fig. 4D). Because most cells undergoing the final stages of apoptosis do not express nuclear markers, we removed all pyknotic γH2AX$^+$ cells from the quantification strategy. Using this approach, we observed significantly more non-pyknotic γH2AX$^+$ cells scattered throughout the E12 U11-null pallium relative to the control (Fig. 4E). Similarly, we observed significantly more cells upregulating p53 throughout the E12 U11-null pallium compared to the control (Fig. 4E). Given the GO-term enriched for by the upregulated protein-coding genes, and reports that p53 stabilization occurs in response to DNA damage (Cheng and Chen, 2010), we expected that most γH2AX$^+$ cells would also upregulate p53. Indeed, 74.7±11.9% of γH2AX$^+$ cells were also upregulating p53 (Fig. 4E, left inset). In contrast, only 6.7±2.0% of p53-upregulating cells were also γH2AX$^+$ (Fig. 4E, right inset). At E11, we observed significantly more γH2AX$^+$ cells in the mutant pallium (2.67±0.76) compared to the control (0%). However, we did not observe a significant difference in the number of p53-upregulating cells in the

control and mutant, suggesting that the precipitation of DNA damage begins at E11, while cell death occurs at E12 (Fig. 4E).

Since the majority of the cells dying between E12 and E13 were self-amplifying RGCs, we next investigated whether RGCs were the cell type accumulating DNA damage and upregulating p53. We found that $46.3\pm3.2\%$ of γH2AX$^+$ cells were Pax6$^+$ RGCs, while virtually none were NeuN$^+$ neurons ($5.1\pm5.1\%$) or Tbr2$^+$ IPCs (0%, Fig. 4F). To test whether RGCs were the primary cell type upregulating p53, we also performed IF for p53 and Pax6. This revealed that the vast majority of p53-upregulating cells were Pax6$^+$ RGCs ($98.1\pm0.85\%$), a significant enrichment compared to the percentage of Pax6$^+$ RGCs found in the mutant pallium ($93.61\pm0.56\%$; Fig. 4G). In all, we found that U11-null RGCs are the primary cell type both accumulating DNA damage and upregulating p53, which most likely contribute to their widespread death between E12 and E13.

U11 loss results in elevated minor intron retention in MIGs that regulate nucleotide binding, protein transport, and cell cycle. Since U11 is an essential component of the minor spliceosome, the expected result of U11 loss is disruption of minor intron splicing. However, none of the genes upregulated in the E12 mutant pallium that enriched for p53-mediated apoptosis contained minor introns, indicating that their upregulation is a secondary effect of U11 loss. Therefore, we next investigated the expression of the minor spliceosome targets, i.e., the MIGs, and the splicing of their minor introns. Overall, the vast majority of MIGs were not differentially expressed (Fig. 4A). Only one MIG, *Spc24*, showed >2-fold downregulation in the mutant (Fig. 4A, arrow), which was independently confirmed by qRT-PCR (Fig. 4C). To assess minor intron splicing, we employed the strategy previously described by (Madan et al., 2015), which utilizes a mis-splicing index (MSI) to reflect intron retention. Using this strategy, we identified 299 (out of 545) minor introns and 11,187 (out of 54,500 randomized major introns) that passed the filtering criteria, indicating that they show some level of intron retention. We then calculated the difference in MSI for each intron between the mutant and the control (mutant MSI − control MSI; ΔMSI) and generated frequency plots (Fig. 5A, Table S3). These revealed a rightward ΔMSI shift for the 299 minor introns, while the 11,187 randomized major introns followed a normal distribution (Table S3). This indicated that loss of U11 inactivates the minor spliceosome, resulting in elevated retention of minor, but not of major, introns.

To identify the specific minor introns with elevated retention in the mutant, we employed student's *t*-tests to compare the MSI of each minor intron between the control and mutant samples. Of the 299 minor introns, we identified 186 minor introns, found in 178 MIGs, with significantly elevated minor intron retention in the mutant (Table S3). For three of these MIGs (*Coa3*, *Parp1*, and *Pten*), this was confirmed by qRT-PCR (Fig. S3A). Minor intron retention has been predicted to result in the introduction of premature stop codons, subsequently targeting MIG transcripts for degradation by the nonsense mediated decay (NMD) pathway (Patel, 2002). To test whether retention of these 186 minor introns would indeed introduce a premature stop codon, we curated a list of all annotated isoforms of these 178 MIGs, and extracted all the isoforms that would require minor intron splicing for

their production, resulting in a list of 330 isoforms (Table S4). Bioinformatics analysis showed that minor intron retention in 99.1% of these isoforms would introduce a stop codon prior to the annotated stop codon (Fig. 5B and Table S4). Since stop codons found >50 nt upstream of an exon-exon junction are predicted to trigger the NMD pathway (Nagy and Maquat, 1998), we also interrogated the location of the premature stop codons in these 330 MIG transcripts in relation to their exon-exon junctions. Again, we found that the majority (83.8%) of the premature stop codons would be predicted to activate NMD, resulting in transcript degradation (Fig. 5B and Table S4). For the remaining 53 MIG transcripts, minor intron retention would introduce a stop codon in the 3' end of the transcript, potentially allowing these transcripts to escape NMD and be translated, resulting in the production of truncated proteins (Fig. 5B inset and Table S4).

Regardless of whether a MIG transcript would be degraded via NMD or would produce an aberrant protein, the functions executed by these MIGs would likely be compromised. To identify which biological processes would be affected in the mutant, we submitted the 178 MIGs with elevated minor intron retention to DAVID (Huang da et al., 2009). Functions significantly enriched for by these MIGs included both broad GO-terms, such as nucleotide binding (36 genes) and protein transport (19 genes), and more specific GO-terms, such as cell cycle (18 genes) and centrosome (13 genes). The enrichment of these more specific functions suggested that aberrant minor intron splicing might result in cell cycle defects (Fig. S3B, Table S5). Moreover, the only downregulated MIG in the mutant pallium, *Spc24*, is involved in kinetochore assembly (Fig. 4A&C, Table S1) (McCleland et al., 2004). In all, disruption of minor intron splicing likely affected cell cycle in the E12 mutant pallium.

U11-null RGCs experience S-phase, prometaphase/metaphase, and cytokinesis defects. Among the 21 cell cycle-regulating MIGs we identified with significantly elevated minor intron retention, there were two noteworthy enrichments: nine MIGs that regulate mitosis and cytokinesis, and six MIGs that regulate S-phase and DNA replication (Table S5). Therefore, we expected that mitosis/cytokinesis and S-phase would likely be affected in the mutant pallium.

To study mitosis in the U11-null pallium, we performed IF for Ki67 and PH3, a marker of mitosis (Gurley et al., 1978), and quantified PH3^{+} mitotic cells as a percentage of the entire Ki67^{+} cycling cell population, to identify the mitotic fraction of the NPC population (Fig. 5C). This quantification revealed a significantly larger mitotic fraction in the E12 mutant pallium relative to the control (Fig. 5C). To investigate whether a specific stage within mitosis was affected in the U11-null E12 pallium, we employed the mitotic marker Aurora B. The staining pattern of Aurora B corresponds to specific phases within mitosis (Sun et al., 2008) (Fig. S4A); by quantifying cells within these specific phases of mitosis, we were able to identify the fraction of mitotic cells in prophase, prometaphase+metaphase, anaphase, and telophase. Aurora B staining was combined with IF for either Pax6 or Tbr2, to assess cell type-specific defects. This staining paradigm revealed a significantly higher percentage of mitotic Aurora B[+]/Pax6^{+} RGCs in prometaphase+metaphase in the E12 mutant pallium than the control, while

prophase, anaphase, and telophase were not significantly different (Fig. 5D-E). In mitotic Tbr2$^+$ IPCs, we did not observe any significant differences in the fractions in prophase, prometaphase+metaphase, anaphase, or telophase (Fig. S4B-C). To investigate cytokinesis in the E12 mutant pallium, we performed IF for citron kinase (Citk), which marks the cytokinetic midbody (Paramasivam et al., 2007). At E12, there was a significant reduction in Citk$^+$ cytokinetic midbodies lining the ventricular edge in the U11-null pallium (Fig. 5F). This reduction was not observed at E11, when the number of Citk$^+$ cytokinetic midbodies across the U11-null pallium was similar to the control (Fig. 5F and S4D). These data suggest that U11 loss causes both prolonged prometaphase/metaphase, specifically in RGCs, and cytokinesis defects.

Next, we explored how minor intron retention in the S phase-regulating MIGs impacted S phase kinetics in the mutant pallium. For this, we pulsed pregnant females with the thymidine analog EdU (Chehrehasa et al., 2009), followed by harvest one hour later. EdU detection revealed a significantly lower percentage of EdU$^+$/Pax6$^+$ RGCs in the mutant compared to the control at E12 (Fig. 5G), while there was no significant difference in the percentage of EdU$^+$/Tbr2$^+$ IPCs between the E12 control and mutant pallium (Fig. 5H). In addition, we observed no change in the percentage of EdU$^+$/Pax6$^+$ RGCs in the E11 mutant pallium compared to the control (Fig. S4E). Thus, U11 loss in RGCs causes S-phase defects at E12, while U11-null IPCs are spared.

Together, these findings indicate that U11 loss disrupts the splicing of MIGs that are involved in mitosis, cytokinesis, and S-phase, resulting in defects in these cell cycle phases. To determine whether other cell cycle phases were affected in the U11-null pallium, we employed the markers cyclin B1, which is cytoplasmic in G2 phase, and Aurora B, which is localized to condensing chromosomes in cells in G2 (Clute and Pines, 1999; Crosio et al., 2002) (Fig. S4A). Neither quantification of cyclin B1$^+$ G2 cells, nor quantification of the percentage of G2 Aurora B$^+$ RGCs or IPCs revealed a significant difference between the E12 mutant and control pallium (Fig. S4B&F-G), further underscoring that U11 loss causes three significant and specific cell cycle defects, affecting (1) prometaphase/metaphase, (2) cytokinesis, and (3) S-phase.

P53 upregulation occurs predominantly in G1 phase. Since the MIGs with significantly elevated minor intron retention enriched for cell cycle functions, we expected that the observed cell cycle defects were the primary cause of RGC death, while the observed DNA damage and p53 upregulation were secondary effects. To determine whether DNA damage and p53 upregulation were occurring in NPCs in S-phase and mitosis/cytokinesis, we combined IF for either γH2AX or p53 with different cell cycle markers. To determine whether cells accruing DNA damage were in S-phase, we employed the aforementioned EdU pulse strategy. IF for γH2AX combined with EdU detection revealed that 38.5±9.3% of γH2AX$^+$ cells were also EdU$^+$, similar to the total percentage of EdU$^+$ cells in the mutant pallium (37.8±1.0%, Fig. 6A). We did not observe any γH2AX$^+$/PH3$^+$ cells in the E12 mutant pallium, indicating that cells with DNA damage were not in mitosis (Fig. S5).

To investigate convergence between p53 upregulation and cell cycle phase, we employed the aforementioned EdU pulse paradigm along with IF for Aurora B. In the E12 mutant pallium, approximately one third (32.5±4.4%) of p53-upregulating cells were also EdU$^+$ (Fig. 6B). However, this enrichment was not statistically significant, when compared to the total percentage of EdU$^+$ cells in the E12 mutant pallium (42.3±1.2%, Fig. 6B). We then leveraged Aurora B to interrogate p53 upregulation in G2 and mitosis. Quantification of cells with G2-specific Aurora B staining in the E12 mutant pallium revealed that 14.4±2.1% of p53-upregulating cells were in G2 phase, a significantly lower percentage than would be expected based on the total percentage of G2 cells in the mutant pallium (26.5±1.4%, Fig. 6C). Similar quantification of mitotic Aurora B$^+$ cells showed that 2.4±0.3% of p53-upregulating cells were mitotic, which was significantly lower than expected from the total percentage of mitotic cells in the mutant pallium (8.5±0.5%, Fig. 6C). Thus, approximately half of p53-upregulating cells were not labeled by these S-, G2-, and M-phase markers, suggesting that these p53-upregulating cells were in G1 phase.

Given that we observed a relationship between p53 upregulation and cell cycle phase, we sought to determine whether apoptosis in U11-null cells was also linked to cell cycle phase. Since pyknotic cells in later stages of apoptosis would not express cell cycle markers, we employed both IF for CC3, to mark cells in early-to-late apoptosis, with TUNEL, to mark cells in late stages of apoptosis . For our analysis, we excluded pyknotic TUNEL$^+$ cells, so that we only considered cells in early stages of apoptosis. First, to investigate S-phase cells, we employed the aforementioned EdU pulse paradigm. Of the CC3$^+$ cells of the E12 mutant pallium, 38.0±19.1% were also EdU$^+$, which was expected based on the total percentage of EdU$^+$ cells in the mutant pallium (42.2±1.2%, Fig. 6D). To assess G2 and mitotic cells, we employed IF for Aurora B. In the E12 mutant pallium, we observed virtually no CC3$^+$/Aurora B$^+$ cells (2.1±2.1%, Fig. 6E), indicative of minimal death of cells in G2 and M phases. Together, these findings indicate a relationship between apoptosis and cell cycle that mirrors that of p53 upregulation and cell cycle: few dying cells are in G2 or M phase, and less than half are in S phase. Therefore, the majority of dying cells in the E12 mutant pallium are most likely in G1 phase or are neurons.

Discussion

Patients with MOPD1, Roifman syndrome, or Lowry Wood syndrome are thought to escape embryonic lethality due to impairment, but not complete inactivation, of minor spliceosome activity. Despite the systemic impairment of minor splicing, the specific phenotypes observed in the brain and limbs of patients indicate tissue/cell-type specific sensitivity to minor spliceosome activity (He et al., 2011; Merico et al., 2015; Farach et al., 2018). Even within the brain, progenitor cells of the cortex are the most sensitive to inhibited minor splicing, as evidenced by the consistent set of cortical abnormalities observed in MOPD1 (Merico et al., 2015). However, investigation into the requirement of minor splicing for cortical development, and whether this requirement is cell type-specific within the cortex has, until now, been unexplored.

Here, we present the first mammalian model of microcephaly caused by minor spliceosome inactivation (Fig. 1D), allowing us to study the pathogenesis of microcephaly in disorders caused by minor spliceosome disruption. Unexpectedly, we found that even within the developing cortex, different cells showed different sensitivities to U11 loss. Specifically, self-amplifying RGCs were highly sensitive to minor spliceosome inactivation, while RGCs undergoing differentiative divisions, IPCs, and neurons were less affected (Fig. 3, S2C-F, 7A). We did not observe a significant difference between the percentage of non-pyknotic BrdU^{+} cells that were NeuN^{+} neurons in the E13 control and mutant pallium, suggesting similar rates of neurogenesis from the control and U11-null NPCs labeled at E12 (Fig. S2F-G). These findings are discordant with the similar numbers of neurons observed in the control and mutant at E13 (Fig. 3D), which may be explained by compensatory neuron production prior to the BrdU pulse. Together, our findings show that minor spliceosome inactivation in the developing mouse cortex predominantly affects the survival of self-amplifying RGCs and may shift RGCs to neurogenic divisions. Ultimately, this would deplete the RGC pool (Fig. 3H & 7A), resulting in the observed microcephaly (Fig. 1D).

In the developing mouse cortex, the U11-null RGCs experience multiple cell cycle defects. For example, fewer U11-null RGCs were in S-phase (Fig. 5G), suggesting faster S-phase progression or death in late G1/early S-phase. U11-null RGCs also displayed prolonged prometaphase/metaphase (Fig. 5C-E), indicative of spindle assembly defects. Since prolongation of mitosis—and particularly of prometaphase/metaphase—has also been linked to increased neurogenic drive in cortical NPCs (Pilaz et al., 2016), this mitotic defect may drive U11-null RGCs to produce neurons. In addition, we observed fewer Citk[+] cytokinetic midbodies along the ventricular edge where RGCs divide, without a change in the fraction of mitotic RGCs in telophase (Fig. 5E-F). This could be caused by RGC death prior to cytokinesis or improper Citk localization to the midbody. Since proper Citk localization is required for cytokinesis, mislocalization would cause aberrant cytokinesis, resulting in RGC death post-division (Di Cunto et al., 2000). In addition to these cell cycle defects, we observed accumulation of DNA damage at E11, followed by further DNA damage accumulation and p53 upregulation in RGCs at E12 (Fig. 4E-G). The majority of RGCs with DNA damage also upregulated p53 (Fig. 4E). Thus, activation of the DNA damage response pathway in these cells likely results in the stabilization of p53 protein, as has been reported (Williams and Schumacher, 2016). However, the vast majority of p53-upregulating RGCs did not have DNA damage, suggesting that DNA damage accumulation is not the sole cause of p53 upregulation and cell death in the mutant pallium (Fig. 4E). For these RGCs, we expect that p53 upregulation is triggered by prometaphase/metaphase prolongation and cytokinesis defects, as has been proposed (Fig. 5C-E) (Uetake and Sluder, 2010; Ganem et al., 2014). This is consistent with the observation that most p53-upregulating cells were not in S-, G2-, or M-phases, suggesting that the majority of p53-upregulating cells were either NPCs in G1 phase or neurons (Fig. 6B-C). Since the vast majority of p53-upregulating cells were Pax6^{+} (Fig. 4G), most of these p53-upregulating cells were likely RGCs in G1 phase (Fig. 6B-C). RNAseq of the pallium revealed that upregulated genes enriched for "intrinsic apoptotic signaling pathway in response to DNA damage by p53 class mediator," which is consistent

with the observed DNA damage and p53 upregulation in RGCs (Fig. 4F-G & Table S2). Two of the genes enriching for this functional category were the well-known p53-mediated apoptosis effectors *Puma* and *Noxa* (Table S2). Upregulation of these p53-mediated apoptosis effectors is likely specific to RGCs, particularly those in G1 phase, since (1) p53 upregulation was observed in RGCs (Fig. 4G&6B-D), and (2) the majority of cells in the E12 pallium are RGCs (Fig. 3E).

In essence, all of these RGC-specific cellular defects are caused by minor spliceosome inactivation—i.e., missplicing of MIGs. In the U11-null pallium, 62% of minor introns were significantly retained compared to the control (Table S3), 21 of which are involved in cell cycle regulation (Fig. S3B & Table S5). Notably, four of these cell cycle-regulating MIGs—*Cdc45*, *Dna2*, *Prim1*, and *Rfc5*—regulate DNA replication and S-phase progression (Table S5); therefore, disruption of their function likely results in DNA damage and cell death in S-phase, which is consistent with the observed cellular defects (Fig. 4D-E, 5G, & 7B). Ineffective DNA damage repair, due to minor intron retention in the 13 MIGs regulating this process (Table S6), would further contribute to DNA damage accumulation and the subsequent p53 upregulation. This pathway may underlie the DNA damage observed in the E11 mutant pallium, prior to p53 upregulation (Fig. 4E & 7B). Disrupted function of many of the remaining cell cycle-regulating MIGs, such as *Ahctf1*, *Dctn3*, *Dync1li1*, *Gak*, *Mau2*, and *Zfp207*, is reported to cause spindle assembly defects, chromosome mis-segregation, and aberrant cytokinesis (Table S5). Thus, minor intron retention in these genes likely contributes to the prolonged prometaphase/metaphase and cytokinesis defects observed in U11-null RGCs at E12, which may in turn trigger the observed p53 upregulation in the absence of DNA damage (Fig. 4E, 5E-F, 7B). The identification of these subsets of MIGs, which show significantly elevated minor intron retention and whose functions track with the observed cellular defects in the U11-null pallium, opens new avenues of research for scientists investigating the pathogenesis of the developmental disorders linked to minor spliceosome inactivation.

Out of the 186 minor introns that showed significantly elevated retention in the U11-null pallium, we predicted that the majority would result in nonsense-mediated decay (Fig. 4B & Table S4). However, none of the 147 MIGs containing these retained minor introns were downregulated in the E12 U11-null pallium (Tables S1 & S4). This is in agreement with the finding that mutation in an essential minor spliceosome protein (rnpc3) in zebrafish did not affect expression levels of 90% of MIGs, while still resulting in elevated minor intron retention (Markmiller et al., 2014). These findings suggest that inactivation of the minor spliceosome, while disrupting minor intron splicing, does not necessarily result in downstream changes in overall gene expression. This could be a result of a transcriptional feedback loop that drives compensatory upregulation of MIG transcription in response to impaired function of these MIGs (Merico et al., 2015). Translation of these transcripts could result in aberrant protein production, with loss- or gain-of-function effects, contributing to the RGC-specific cellular defects and death.

In both the U11-null pallium and in MOPD1 patients, the observed differential sensitivity to minor spliceosome inactivation may be informed by differences in MIG expression across cell types, where higher MIG expression is correlated with increased sensitivity to minor spliceosome inactivation. Furthermore, if minor introns themselves display differential sensitivity to minor spliceosome inactivation, as our data suggest (Table S3), then the identity of MIGs expressed in specific cell types could inform that cell type's susceptibility to minor spliceosome inactivation. In all, our findings establish how minor spliceosome inactivation in the developing mammalian cortex leads to microcephaly. Moreover, we are the first to identify cell type-specific requirements for minor spliceosome activity within the developing cortex, raising new questions about the mechanisms underlying cell type-specific sensitivity to minor spliceosome activity in mammalian development and disease.

Materials and Methods

Animal Procedures and Generation of the *Rnu11* cKO Mouse

All mouse procedures were performed according to the protocols approved by the University of Connecticut Institutional Animal Care and Use Committee. The *Rnu11* conditional knockout (cKO) mouse was generated by the University of Connecticut Health Center. A single targeting construct was utilized to introduce both loxP sites into the *Rnu11* locus in mouse embryonic stem (ES) cells (Fig. S1A). This construct contained a 5' loxP site 1090 bp from the *Rnu11* gene. Immediately upstream of the 3' loxP site was a phosphoglycerine kinase (PGK)-Neomycin (Neo) cassette flanked by Frt sites. Additionally, this construct contained a PGK-dTA (diphtheria toxin A) negative selection cassette downstream of the 3' arm of homology. This construct was electroporated into 129X1/SvJ mouse embryonic stem (ES) cells. Successful targeting was verified by G418-mediated positive selection. Subsequently, nested long-range PCR was employed to confirm successful homologous recombination at both the 5' and 3' loxP sites (Fig. S1C). Two ES-cell clones, F4 and H8, were then used for morula aggregation using C57BL/6 embryos to generate a chimera. Germline transmission and ablation of the Neo cassette was verified by introducing germline Flp recombinase. Proper loxP site placement in the resulting mouse line was confirmed by PCR (Fig. 1A; Table S7) to identify loss of the wild-type allele in the homozygous floxed line and by breeding in the germline *EIIa*-Cre (Lakso et al., 1996) (Fig. 1A). *Emx1*-Cre was bred into the *Rnu11* conditional knockout line to target *Rnu11* for removal in the developing forebrain (Gorski et al., 2002). The primers used for *Rnu11*, Cre, and *Emx1*-Cre zygosity genotyping PCRs are listed in Table S7. All experiments were performed using male and female *Rnu11*$^{WT/Flx}$ and *Rnu11*$^{Flx/Flx}$ mice that were *Emx1*-Cre$^{+/-}$. For matings intended for embryonic harvests, the plug date was considered E0; on the harvest date, the embryonic time-point was further verified by Theiler staging of the embryos.

Quantitative PCR

Quantitative PCR (qPCR) using Genomic DNA To determine *Rnu11* heterozygosity and loss of the WT allele, 25 ng of gDNA from *Rnu11*$^{WT/KO}$ and *Rnu11*$^{WT/WT}$ mice was used for qPCR with *Rnu11* cKO, 5' loxP primers (Table S7). Equal gDNA input was controlled with amplification for *Hist1h1a*, an intronless gene, which was then used to normalize amplification for *Rnu11*.

Quantitative Reverse-Transcriptase PCR (qRT-PCR) Loss of U11 expression was confirmed by qRT-PCR with U11 primers (Table S7) on cDNA prepared from total RNA extracted from the pallium of control (*N*=3) and mutant (*N*=4) E12 embryos. In this case, *Neat1*, a non-coding RNA that did not show change in expression between the control and mutant samples by RNAseq, was used to normalize expression of U11 by qRT-PCR (Hutchinson et al., 2007) (Table S1). The same cDNA was used to determine expression of *Spc24*, using primers designed in the 3' UTR of the gene (Table S7). The Cq values obtained for *Sfrs10* (Table S7) were used to normalize expression of *Spc24* (Banday et al., 2014). For minor intron retention in *Coa3*, *Parp1*, and *Pten*, expression values of exon-intron (unspliced) product were normalized using Cq values generated using intergenic primers (Table S7) to offset any gDNA contamination (Banday et al. 2014). Expression values of exon-exon (spliced) product were normalized using *Sfrs10* Cq values (Banday et al., 2014). Minor intron retention for each of these MIGs was calculated by dividing the normalized fold expression values of the unspliced product by the normalized fold expression values of the spliced product. Statistical significance was determined by two-tailed student's *t*-tests (Table S8).

Hematoxylin and Eosin Staining

Frozen 16 µm coronal sections of P0 mouse brains were cured at room temperature for 15 minutes, followed by incubation in PBS for 15 minutes. The tissue was then dehydrated using an ethanol gradient (25%, 50%, and 75%). Slides were washed twice in 100% ethanol for 30 seconds each, with agitation, then washed twice in 95% ethanol for 30 seconds each, with agitation. Following a rinse in running tap water, the sections were incubated in Harris hematoxylin (Fisher Scientific, #6765001) for 7 minutes. Excess hematoxylin was removed by washing in running water for 30 seconds. The slides were briefly agitated in 1% acid alcohol (1% HCl in ethanol), then briefly rinsed in running water. Sections were then incubated for 2-3 minutes in saturated lithium carbonate (1.54% in dH$_2$O), followed by a 5-minute incubation in tap water. After a 30 second wash in 80% ethanol with agitation, slides were incubated in an eosin Y-phloxine B solution (0.1% eosin Y, 0.01% phloxine B, 0.45% glacial acetic acid, 82.9% ethanol) for 1 minute. The sections were then washed in 95% ethanol for 30 seconds with agitation, followed by two 30-second washes in 100% ethanol with agitation and incubation in 100% ethanol for 1 minute. After washing in xylene for 30 seconds with agitation, the slides were washed in xylene for 1 minute, then mounted using Permount^{TM} mounting medium (Fisher Scientific, #SP15-100).

In Situ Hybridization

16 µm cryosections of mouse heads (for E10–E12 and P0), telencephalons (E13–E14), and whole brains (for P21), *N*=3 for each time-point and genotype, were used for section *in situ* hybridization (SISH). SISH was performed using antisense, digoxigenin-labeled U11 RNA probe, which was detected using either alkaline phosphatase (AP) or fluorescent labeling (FISH), as described in (Baumgartner et al., 2014). The U11 probe was generated using the U11 expression primers in Table S7.

TUNEL Assay

16 µm cryosections of either embryonic mouse heads (for E10 – E12) or telencephalons (E13 – E14) were used for terminal deoxynucleotidyl transferase dUTP nick ending labeling (TUNEL) analysis. The *in situ* cell death detection kit, TMR red (Roche, #12156792910), was used, according to the manufacturer's instructions.

Immunofluorescence

Immunofluorescence was performed using one of three protocols. Staining for Tbr2 was performed as described by (Arno et al., 2014). For staining with anti-NeuN antibody, heat-mediated antigen retrieval was performed using citrate buffer, per the manufacturer's instructions (Vector Laboratories, #H-3300), followed by 10 minute PBS washes (3x). After three 10 minute washes in 0.5% Triton® X-100 in PBS (PBT), sections were incubated in 10% FBS in PBS for one hour at room temperature. Sections were then incubated in a PBS solution containing 1% FBS, 0.1% Triton® X-100, and the primary antibody overnight at 4°C. Following five-minute washes in PBT (10x), incubation with the secondary antibody (1:500) was performed similarly to the primary antibody incubation, except for two hours at room temperature. The slides were then washed five times with PBT, followed by three PBS washes and mounting with ProLong® Gold Antifade Mountant (ThermoFisher Scientific, #P36930). For all other antibodies, staining was performed as described in (Karunakaran et al., 2015). Primary antibodies were diluted to 1:50 (mouse anti-CRIK/CITK, BD Biosciences, #611376; rabbit anti-cyclin B1, Cell Signaling, #4138; MoBu-1 clone mouse anti-BrdU, Santa Cruz, #sc-51514), 1:100 (mouse anti-Aurora-B/AIM1, BD Biosciences, #611082; mouse anti-Pax6, Developmental Studies Hybridoma Bank, #PAX6-b), 1:200 (mouse anti-γH2AX, MilliporeSigma, #05-636; rabbit anti-NeuN, abcam, #ab17787), 1:300 (rabbit anti-cleaved caspase 3, Cell Signaling, #9665S; mouse anti-KI67, BD Biosciences, #556003; rabbit anti-p53, Leica Microsystems, #p53-CM5p; rabbit anti-Pax6, MilliporeSigma, #AB2237), or 1:500 (rabbit anti-PH3, Bethyl Laboratories, Inc., #IHC-00061; rabbit anti-TBR2, abcam, #ab23345).

5-bromo-2'-deoxyuridine (BrdU) and 5-ethynyl-2'deoxyuridine (EdU) Pulse Experiments

Timed-pregnant $Rnu11^{WT/Flx}$::$Emx1$-Cre$^{+/+}$ females were first weighed and peritoneally injected with 0.2 µL 25 mM BrdU or EdU in PBS per 100 mg body weight, one hour prior to embryonic harvest. BrdU incorporation was detected using the BrdU-specific MoBu-1 clone anti-BrdU antibody (Santa Cruz, #sc-51514) (Liboska et al., 2012). EdU detection was then performed on sections of the pallium, using the Click-iT^{TM} EdU Alexa Fluor^{TM} 647 imaging kit (ThermoFisher Scientific, #C10340) in accordance with the manufacturer's instructions.

Image Acquisition and Quantification

Processed slides were imaged with a Leica SP2 confocal microscope, where settings for laser intensity, excitation-emission windows, gain, and offset conditions were identical between control and mutant sections on a given slide. For every slide that was processed for ISH, FISH, or IF, the slide contained at least one control and one mutant section. Sections serial to those that revealed loss of U11 by ISH analysis were used for IF staining, and images were collected in regions of the pallium that showed U11 loss in the mutant by ISH (Fig. 1E). For each channel for every experimental condition, confocal imaging settings were optimized for fluorescence in the control section on a given slide, and maintained for all other sections on that slide. For TUNEL, CC3, γH2AX, and p53 imaging, collection settings were adjusted using the control section. These settings were maintained when imaging the mutant section(s) on the same slide. Further processing was performed on IMARIS v8.3.1 (Bitplane Inc.) and Adobe Photoshop CS4 (Adobe Systems Inc.). All image processing in IMARIS and Photoshop was identical between images of control and mutant sections from the same slide. Manual quantification was performed using the spot tool in the IMARIS software, on 240 µm-wide columns of the pallium; statistical significance was calculated using two-tailed student's t-tests (Table S8). For quantification of mitotic phases, as identified by Aurora B staining (Fig. S4A), prometaphase and metaphase cells were summed together into a single category (prometaphase/metaphase). For analysis of Pax6^{+} and Tbr2^{+} cell quantification across mutant cortical development, statistical significance was determined by one-way ANOVA, followed by the post hoc Tukey test (Table S8). For comparisons between the γH2AX^{+}, p53^{+}, or CC3^{+} subpopulation and all DAPI^{+} cells in the E12 mutant pallium, statistical significance was determined by Fisher exact test (Table S8). Specifically, for each N, a separate Fisher exact test was performed on quantification data from a 240 µm-wide column of the mutant pallium. The P values from these Fisher exact tests were then combined using Fisher's method (Table S8).

Bioinformatics Analysis

RNAseq The pallium was dissected from E12 (*N*=5 *Rnu11*$^{WT/Flx}$ *Emx1*-Cre$^{+/-}$, *N*=5 *Rnu11*$^{Flx/Flx}$::*Emx1*-Cre$^{+/-}$) embryos, followed by RNA extraction using TRIzol (Thermo Fisher Scientific, #15596018), per the manufacturer's instructions. Sample preparation and sequencing were performed by the University of Connecticut Center for Genome Innovation. Total RNA library was prepared by Illumina TruSeq Stranded Total RNA Library Sample Prep Kit (RS-122-2201) with Ribozero to remove ribosomal RNA, and were then sequenced using Illumina NextSeq 500. Each sample was barcoded so that the sequencing could be multiplexed. In total, we obtained 189,989,434 paired-end 151 bp reads for the control (*N*=5) and 219,849,711 paired-end 151 bp reads for the mutant samples (*N*=5).

Gene expression First, reads of individual replicates were merges and mapped to the mm10 genome (UCSC genome browser) using Hisat2 (options –no-discordant and –no-mixed), with an overall alignment rate of 85% (Kim et al., 2015). Reads that mapped to multiple locations in the genome were removed. Since the samples were obtained from C57BL/6-129X1/SvJ mice, SNVQ was run to call single nucleotide variations (SNVs) (Duitama et al., 2012), which were used to create a new reference genome. Reads from all replicates were then mapped separately to the newly generated reference genome using Hisat2. Isoform expression was determined by IsoEM2, an expectation-maximization algorithm that bootstraps samples in order to determine an expression value in fragments per kilobase per million mapped reads (FPKM) unit (Mandric et al., 2017). Gene expression was then calculated by taking the sum of the FPKM values of a given gene's constituent isoforms. Finally, differential gene expression (≥2 fold change, *P*≤0.01) was determined by IsoDE2 (Mandric et al., 2017). Briefly, this tool utilizes the 200 bootstrapping iterations to compute a confident log2FC, which is the maximum log2FC that can be computed within the specified *P*-value. A log2FC of 100 is reported when the FPKM value for one of the conditions was 0 in one of the bootstrapping iterations.

Splicing efficiency To assess minor intron splicing, sequences of the 555 minor introns were curated from the U12DB (Alioto, 2007) and blasted using Ensembl83 to obtain the minor intron coordinates in the canonical transcript. Sequences of eight minor introns (found in *Arpc5l, Cacna1c, Exosc2, Golga7, Ift80, Mlst8, Tmem161b,* and *Morc4*) that did not have 100% identity with any annotated intron in the Ensembl database were removed from our analysis. All gene and exon coordinates from the mm10 genome were obtained from a Biomart file (Ensembl v84). Major intron coordinates were downloaded from the UCSC genome browser (Ensembl v84) and randomized after removal of introns smaller than 4 nt.

Reads from each of the biological replicates were separately mapped with Hisat2 to the previously described post-SNVQ generated reference genome. Reads that mapped to multiple locations were then filtered out. To determine splicing efficiency of minor introns, we employed the strategy described by (Madan et al., 2015). Briefly, all reads mapping to an exon-intron boundary were extracted and quantified using BEDTools (Quinlan and Hall, 2010). The mis-splicing index (MSI) was then calculated for each intron by dividing the number of exon-intron junction reads by the number of reads mapping to the canonical exon-exon splice-

junctions. Only introns with >4 exon-intron boundary reads, ≥1 read aligning to either the 5' or 3' splice site, and >95% intron coverage in at least one sample were used for this analysis (Madan et al., 2015). As a control for the 545 minor introns subjected to these criteria, we also generated 100 lists of 545 randomized major introns (54,500 randomized major introns in total), to which we applied the same criteria. For each intron that passed the filtering criteria, we calculated the difference between the mutant and the control (mutant MSI – control MSI; ∆MSI). To determine which minor introns were retained significantly more in the mutant, we compared the average MSI of each minor intron between the control and mutant samples using two-tailed student's *t*-tests (Table S3).

ORF analysis To analyze the effect of minor intron retention on the ORF, we curated all annotated isoforms of the 178 MIGs containing minor introns with significantly elevated retention in the mutant from Ensembl (v84). From this list of isoforms, we extracted only isoforms that would require minor intron splicing for their production, i.e. the blasted minor intron coordinates match one of the annotated intron coordinates 100%, resulting in 330 isoforms. Comparison of the annotated open reading frame (ORF) sequence, with the sequence of the isoform containing a retained minor intron, was performed to determine whether minor intron retention would result in introduction of a premature stop codon in these isoforms. Isoforms were then binned into one of four categories: (1) truncation of the ORF, due to a premature stop codon; (2) elongation of the ORF, with usage of a premature stop codon; (3) elongation of the ORF, with usage of the isoform's annotated stop codon; and (4) no change in ORF size, with usage of a premature stop codon (Table S4). For the 273 isoforms binned in category (1), we identified the location of the stop codon relative to the downstream exon-exon junction. Based on this information, we further subdivided isoforms from category (1) into (a) isoforms with premature stop codons >50 nt upstream of an exon-exon junction, which would be predicted to activate nonsense mediated decay (NMD) of the transcript (Nagy and Maquat, 1998); and (b) isoforms with premature stop codons >50 nt upstream of an exon-exon junction, which might escape NMD and be used for protein production (Table S4).

RNA Extraction and cDNA Preparation.

Palliums were dissected from E12 *Rnu11* control (*N*=3) and mutant (*N*=4) mice, and the tissue collected from each embryo was individually used for total RNA isolation. Tissue from each embryo was separately triturated in 100 µL of TRIzol (Invitrogen, #15596026). RNA was extracted using the DirectZOL^{TM} RNA MiniPrep kit (Zymo Research, #R2050), per the manufacturer's instructions. For total RNA samples, 500 ng of RNA was used for cDNA synthesis, which was performed as previously described in (Baumgartner et al., 2014).

Declaration of Interests

The authors declare no competing interests.

Data Availability

The RNAseq data analyzed in this paper are available in the NCBI Gene Expression Omnibus (GEO) Database, under the accession number GSE96616.

References

Alioto, T. S. (2007) 'U12DB: a database of orthologous U12-type spliceosomal introns', *Nucleic Acids Res* 35(Database issue): D110-5.

Arno, B., Grassivaro, F., Rossi, C., Bergamaschi, A., Castiglioni, V., Furlan, R., Greter, M., Favaro, R., Comi, G., Becher, B. et al. (2014) 'Neural progenitor cells orchestrate microglia migration and positioning into the developing cortex', *Nat Commun* 5: 5611.

Banday, A. R., Baumgartner, M., Al Seesi, S., Karunakaran, D. K., Venkatesh, A., Congdon, S., Lemoine, C., Kilcollins, A. M., Mandoiu, I., Punzo, C. et al. (2014) 'Replication-dependent histone genes are actively transcribed in differentiating and aging retinal neurons', *Cell Cycle* 13(16): 2526-41.

Bartolini, G., Ciceri, G. and Marin, O. (2013) 'Integration of GABAergic interneurons into cortical cell assemblies: lessons from embryos and adults', *Neuron* 79(5): 849-64.

Baumgartner, M., Lemoine, C., Al Seesi, S., Karunakaran, D. K., Sturrock, N., Banday, A. R., Kilcollins, A. M., Mandoiu, I. and Kanadia, R. N. (2014) 'Minor splicing snRNAs are enriched in the developing mouse CNS and are crucial for survival of differentiating retinal neurons', *Dev Neurobiol*.

Calegari, F. and Huttner, W. B. (2003) 'An inhibition of cyclin-dependent kinases that lengthens, but does not arrest, neuroepithelial cell cycle induces premature neurogenesis', *J Cell Sci* 116(Pt 24): 4947-55.

Chehrehasa, F., Meedeniya, A. C., Dwyer, P., Abrahamsen, G. and Mackay-Sim, A. (2009) 'EdU, a new thymidine analogue for labelling proliferating cells in the nervous system', *J Neurosci Methods* 177(1): 122-30.

Cheng, Q. and Chen, J. (2010) 'Mechanism of p53 stabilization by ATM after DNA damage', *Cell Cycle* 9(3): 472-8.

Clute, P. and Pines, J. (1999) 'Temporal and spatial control of cyclin B1 destruction in metaphase', *Nat Cell Biol* 1(2): 82-7.

Crosio, C., Fimia, G. M., Loury, R., Kimura, M., Okano, Y., Zhou, H., Sen, S., Allis, C. D. and Sassone-Corsi, P. (2002) 'Mitotic phosphorylation of histone H3: spatio-temporal regulation by mammalian Aurora kinases', *Mol Cell Biol* 22(3): 874-85.

Di Cunto, F., Imarisio, S., Hirsch, E., Broccoli, V., Bulfone, A., Migheli, A., Atzori, C., Turco, E., Triolo, R., Dotto, G. P. et al. (2000) 'Defective neurogenesis in citron kinase knockout mice by altered cytokinesis and massive apoptosis', *Neuron* 28(1): 115-27.

Duitama, J., Srivastava, P. K. and Mandoiu, II (2012) 'Towards accurate detection and genotyping of expressed variants from whole transcriptome sequencing data', *BMC Genomics* 13 Suppl 2: S6.

Englund, C., Fink, A., Lau, C., Pham, D., Daza, R. A., Bulfone, A., Kowalczyk, T. and Hevner, R. F. (2005) 'Pax6, Tbr2, and Tbr1 are expressed sequentially by radial glia, intermediate progenitor cells, and postmitotic neurons in developing neocortex', *J Neurosci* 25(1): 247-51.

Faleiro, L., Kobayashi, R., Fearnhead, H. and Lazebnik, Y. (1997) 'Multiple species of CPP32 and Mch2 are the major active caspases present in apoptotic cells', *EMBO J* 16(9): 2271-81.

Farach, L. S., Little, M. E., Duker, A. L., Logan, C. V., Jackson, A., Hecht, J. T. and Bober, M. (2018) 'The expanding phenotype of RNU4ATAC pathogenic variants to Lowry Wood syndrome', *Am J Med Genet A* 176(2): 465-469.

Ganem, N. J., Cornils, H., Chiu, S. Y., O'Rourke, K. P., Arnaud, J., Yimlamai, D., Thery, M., Camargo, F. D. and Pellman, D. (2014) 'Cytokinesis failure triggers hippo tumor suppressor pathway activation', *Cell* 158(4): 833-848.

Gorski, J. A., Talley, T., Qiu, M., Puelles, L., Rubenstein, J. L. and Jones, K. R. (2002) 'Cortical excitatory neurons and glia, but not GABAergic neurons, are produced in the Emx1-expressing lineage', *J Neurosci* 22(15): 6309-14.

Gotz, M. and Huttner, W. B. (2005) 'The cell biology of neurogenesis', *Nat Rev Mol Cell Biol* 6(10): 777-88.

Gotz, M., Stoykova, A. and Gruss, P. (1998) 'Pax6 controls radial glia differentiation in the cerebral cortex', *Neuron* 21(5): 1031-44.

Grant, E., Hoerder-Suabedissen, A. and Molnar, Z. (2012) 'Development of the corticothalamic projections', *Front Neurosci* 6: 53.

Gurley, L. R., D'Anna, J. A., Barham, S. S., Deaven, L. L. and Tobey, R. A. (1978) 'Histone phosphorylation and chromatin structure during mitosis in Chinese hamster cells', *Eur J Biochem* 84(1): 1-15.

He, H., Liyanarachchi, S., Akagi, K., Nagy, R., Li, J., Dietrich, R. C., Li, W., Sebastian, N., Wen, B., Xin, B. et al. (2011) 'Mutations in U4atac snRNA, a component of the minor spliceosome, in the developmental disorder MOPD I', *Science* 332(6026): 238-40.

Homem, C. C., Repic, M. and Knoblich, J. A. (2015) 'Proliferation control in neural stem and progenitor cells', *Nat Rev Neurosci* 16(11): 647-59.

Huang da, W., Sherman, B. T. and Lempicki, R. A. (2009) 'Systematic and integrative analysis of large gene lists using DAVID bioinformatics resources', *Nat Protoc* 4(1): 44-57.

Hutchinson, J. N., Ensminger, A. W., Clemson, C. M., Lynch, C. R., Lawrence, J. B. and Chess, A. (2007) 'A screen for nuclear transcripts identifies two linked noncoding RNAs associated with SC35 splicing domains', *BMC Genomics* 8: 39.

Karunakaran, D. K., Chhaya, N., Lemoine, C., Congdon, S., Black, A. and Kanadia, R. (2015) 'Loss of citron kinase affects a subset of progenitor cells that alters late but not early neurogenesis in the developing rat retina', *Invest Ophthalmol Vis Sci* 56(2): 787-98.

Kim, D., Langmead, B. and Salzberg, S. L. (2015) 'HISAT: a fast spliced aligner with low memory requirements', *Nat Methods* 12(4): 357-60.

Kolossova, I. and Padgett, R. A. (1997) 'U11 snRNA interacts in vivo with the 5' splice site of U12-dependent (AU-AC) pre-mRNA introns', *RNA* 3(3): 227-33.

Kowalczyk, T., Pontious, A., Englund, C., Daza, R. A., Bedogni, F., Hodge, R., Attardo, A., Bell, C., Huttner, W. B. and Hevner, R. F. (2009) 'Intermediate neuronal progenitors (basal progenitors) produce pyramidal-projection neurons for all layers of cerebral cortex', *Cereb Cortex* 19(10): 2439-50.

Kyrylkova, K., Kyryachenko, S., Leid, M. and Kioussi, C. (2012) 'Detection of apoptosis by TUNEL assay', *Methods Mol Biol* 887: 41-7.

Lakso, M., Pichel, J. G., Gorman, J. R., Sauer, B., Okamoto, Y., Lee, E., Alt, F. W. and Westphal, H. (1996) 'Efficient in vivo manipulation of mouse genomic sequences at the zygote stage', *Proc Natl Acad Sci U S A* 93(12): 5860-5.

Lange, C., Huttner, W. B. and Calegari, F. (2009) 'Cdk4/cyclinD1 overexpression in neural stem cells shortens G1, delays neurogenesis, and promotes the generation and expansion of basal progenitors', *Cell Stem Cell* 5(3): 320-31.

Liboska, R., Ligasova, A., Strunin, D., Rosenberg, I. and Koberna, K. (2012) 'Most anti-BrdU antibodies react with 2'-deoxy-5-ethynyluridine -- the method for the effective suppression of this cross-reactivity', *PLoS One* 7(12): e51679.

Madan, V., Kanojia, D., Li, J., Okamoto, R., Sato-Otsubo, A., Kohlmann, A., Sanada, M., Grossmann, V., Sundaresan, J., Shiraishi, Y. et al. (2015) 'Aberrant splicing of U12-type introns is the hallmark of ZRSR2 mutant myelodysplastic syndrome', *Nat Commun* 6: 6042.

Mandric, I., Temate-Tiagueu, Y., Shcheglova, T., Al Seesi, S., Zelikovsky, A. and Mandoiu, II (2017) 'Fast bootstrapping-based estimation of confidence intervals of expression levels and differential expression from RNA-Seq data', *Bioinformatics* 33(20): 3302-3304.

Markmiller, S., Cloonan, N., Lardelli, R. M., Doggett, K., Keightley, M. C., Boglev, Y., Trotter, A. J., Ng, A. Y., Wilkins, S. J., Verkade, H. et al. (2014) 'Minor class splicing shapes the zebrafish transcriptome during development', *Proc Natl Acad Sci U S A* 111(8): 3062-7.

McCleland, Mark L, Kallio, Marko J, Barrett-Wilt, Gregory A, Kestner, Cortney A, Shabanowitz, Jeffrey, Hunt, Donald F, Gorbsky, Gary J and Stukenberg, P Todd (2004) 'The vertebrate Ndc80 complex contains Spc24 and Spc25 homologs, which are required to establish and maintain kinetochore-microtubule attachment', *Current biology* 14(2): 131-137.

Merico, D., Roifman, M., Braunschweig, U., Yuen, R. K., Alexandrova, R., Bates, A., Reid, B., Nalpathamkalam, T., Wang, Z., Thiruvahindrapuram, B. et al. (2015) 'Compound heterozygous mutations in the noncoding RNU4ATAC cause Roifman Syndrome by disrupting minor intron splicing', *Nat Commun* 6: 8718.

Nagy, E. and Maquat, L. E. (1998) 'A rule for termination-codon position within intron-containing genes: when nonsense affects RNA abundance', *Trends Biochem Sci* 23(6): 198-9.

Noctor, S. C., Martinez-Cerdeno, V., Ivic, L. and Kriegstein, A. R. (2004) 'Cortical neurons arise in symmetric and asymmetric division zones and migrate through specific phases', *Nat Neurosci* 7(2): 136-44.

Paramasivam, M., Chang, Y. J. and LoTurco, J. J. (2007) 'ASPM and citron kinase co-localize to the midbody ring during cytokinesis', *Cell Cycle* 6(13): 1605-12.

Patel, A. A. and Steitz, J. A. (2003) 'Splicing double: insights from the second spliceosome', *Nat Rev Mol Cell Biol* 4(12): 960-70.

Pilaz, L. J., McMahon, J. J., Miller, E. E., Lennox, A. L., Suzuki, A., Salmon, E. and Silver, D. L. (2016) 'Prolonged Mitosis of Neural Progenitors Alters Cell Fate in the Developing Brain', *Neuron* 89(1): 83-99.

Pilaz, L. J., Patti, D., Marcy, G., Ollier, E., Pfister, S., Douglas, R. J., Betizeau, M., Gautier, E., Cortay, V., Doerflinger, N. et al. (2009) 'Forced G1-phase reduction alters mode of division, neuron number, and laminar phenotype in the cerebral cortex', *Proc Natl Acad Sci U S A* 106(51): 21924-9.

Quinlan, A. R. and Hall, I. M. (2010) 'BEDTools: a flexible suite of utilities for comparing genomic features', *Bioinformatics* 26(6): 841-2.

Scholzen, T. and Gerdes, J. (2000) 'The Ki-67 protein: from the known and the unknown', *J Cell Physiol* 182(3): 311-22.

Sharma, A., Singh, K. and Almasan, A. (2012) 'Histone H2AX phosphorylation: a marker for DNA damage', *Methods Mol Biol* 920: 613-26.

Siegenthaler, J. A. and Pleasure, S. J. (2011) 'We have got you 'covered': how the meninges control brain development', *Curr Opin Genet Dev* 21(3): 249-55.

Sun, L., Gao, J., Dong, X., Liu, M., Li, D., Shi, X., Dong, J. T., Lu, X., Liu, C. and Zhou, J. (2008) 'EB1 promotes Aurora-B kinase activity through blocking its inactivation by protein phosphatase 2A', *Proc Natl Acad Sci U S A* 105(20): 7153-8.

Takahashi, T., Nowakowski, R. S. and Caviness, V. S., Jr. (1995) 'The cell cycle of the pseudostratified ventricular epithelium of the embryonic murine cerebral wall', *J Neurosci* 15(9): 6046-57.

Tarn, W. Y. and Steitz, J. A. (1996a) 'Highly diverged U4 and U6 small nuclear RNAs required for splicing rare AT-AC introns', *Science* 273(5283): 1824-32.

Tarn, W. Y. and Steitz, J. A. (1996b) 'A novel spliceosome containing U11, U12, and U5 snRNPs excises a minor class (AT-AC) intron in vitro', *Cell* 84(5): 801-11.

Uetake, Y. and Sluder, G. (2010) 'Prolonged prometaphase blocks daughter cell proliferation despite normal completion of mitosis', *Curr Biol* 20(18): 1666-71.

Williams, A. B. and Schumacher, B. (2016) 'p53 in the DNA-Damage-Repair Process', *Cold Spring Harb Perspect Med* 6(5).

Wolf, H. K., Buslei, R., Schmidt-Kastner, R., Schmidt-Kastner, P. K., Pietsch, T., Wiestler, O. D. and Blumcke, I. (1996) 'NeuN: a useful neuronal marker for diagnostic histopathology', *J Histochem Cytochem* 44(10): 1167-71.

Zhang, J. and Jiao, J. (2015) 'Molecular Biomarkers for Embryonic and Adult Neural Stem Cell and Neurogenesis', *Biomed Res Int* 2015: 727542.
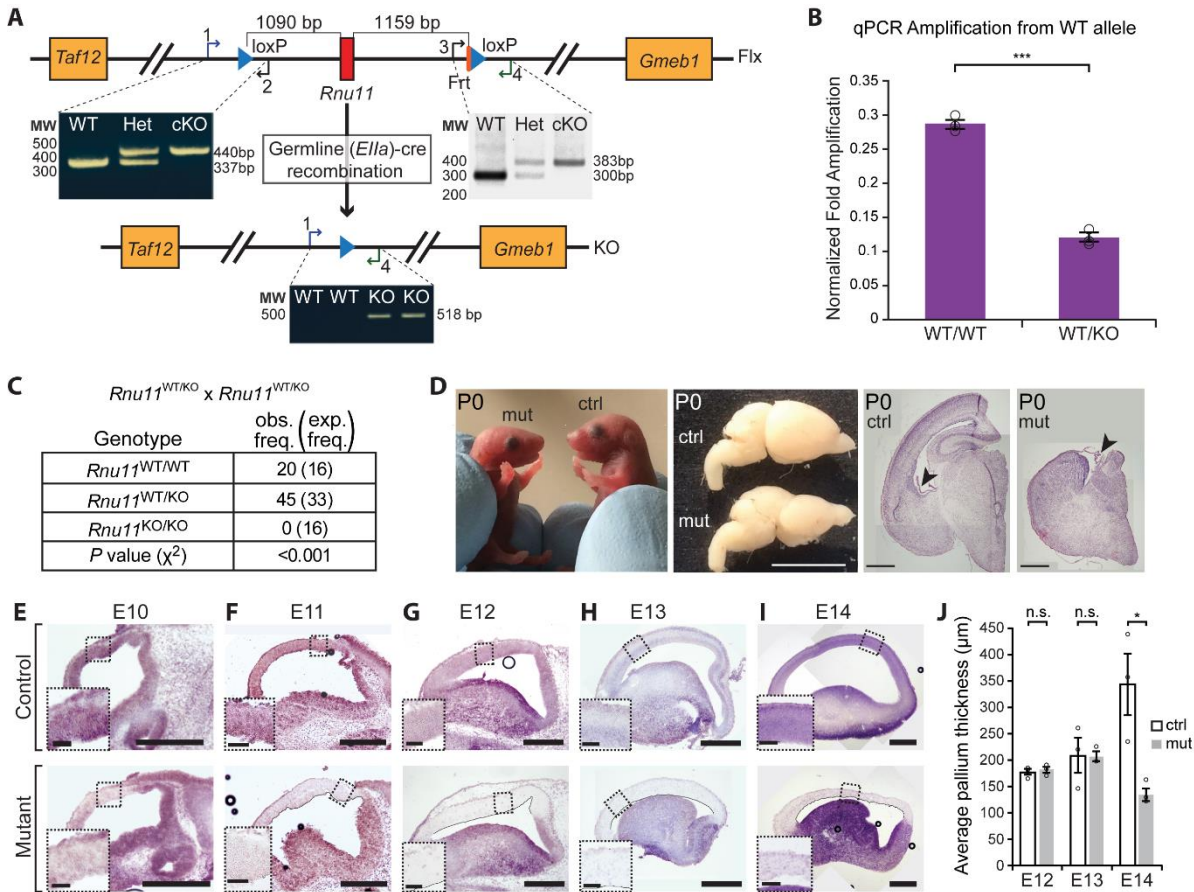
Figures

Figure 1. U11 loss in the developing mouse neocortex causes severe microcephaly. (**A**) Schematic of the *Rnu11* floxed (Flx) allele with positions of the loxP sites (blue triangles), with agarose gel image showing PCR results detecting the upstream (left) and downstream (right) loxP sites. Below is a schematic of the *Rnu11* knockout (KO) allele, confirmed by PCR. See also Fig. S1 and Table S7. (**B**) Results of quantitative PCR (qPCR) detecting the WT allele. See also Table S7. (**C**) Table showing genotype frequency of pups produced from crosses of *Rnu11*[WT/KO] mice. (**D**) Images of P0 *Rnu11*[WT/Flx]::*Emx1*-Cre^{+/-} (control, ctrl) and *Rnu11*[Flx/Flx]::*Emx1*-Cre^{+/-} (mutant, ctrl) pups, with lateral view of P0 ctrl and mut brains. Scale bar=5 mm. At right are coronal sections of P0 ctrl and mut brains stained with hematoxylin and eosin. Arrowheads indicate the choroid plexis. Scale bar=500 µm. (**E-I**) *In situ* hybridization (ISH) for U11 expression (purple signal) in sagittal sections of the telencephalon from ctrl (top row) and mut (bottom row) (**E**) E10, (**F**) E11, (**G**) E12, (**H**) E13, and (**I**) E14 embryos. Scale bars=500 µm. Insets show higher magnification of the boxed regions; scale bars=200 µm. (**J**) Bar graphs showing the average thickness of the E12, E13, and E14 ctrl and mut pallium. Quantification data are represented as mean±SEM. For details of statistical methods, see Table S8. n.s.=not significant; *=$P<0.05$; ***=$P<0.001$
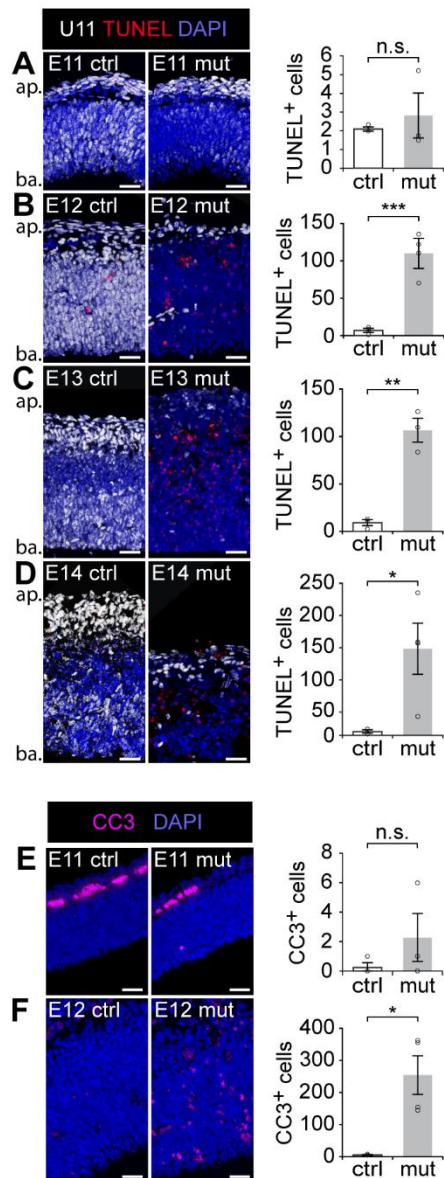
Figure 2. Cell death contributes to microcephaly in the U11 cKO. (**A-E**) Fluorescent ISH (FISH) signal for U11 (white) combined with TUNEL (red) on control (ctrl, left) and mutant (mut, middle) pallium sections from (**A**) E11, (**B**) E12, (**C**) E13, and (**D**) E14 embryos, with quantification of TUNEL$^+$ cells (right). Ap=apical; ba=basal. (**E-F**) Immunofluorescence (IF) for cleaved caspase 3 (CC3) in ctrl (left) and mut (middle) pallium sections from (**E**) E11 and (**F**) E12 embryos, with quantification of CC3$^+$ cells (right). Scale bars=30 µm. Data are represented as mean±SEM. For details of statistical methods, see Table S8. n.s.=not significant; *=$P<0.05$; **=$P<0.01$; ***=$P<0.001$.
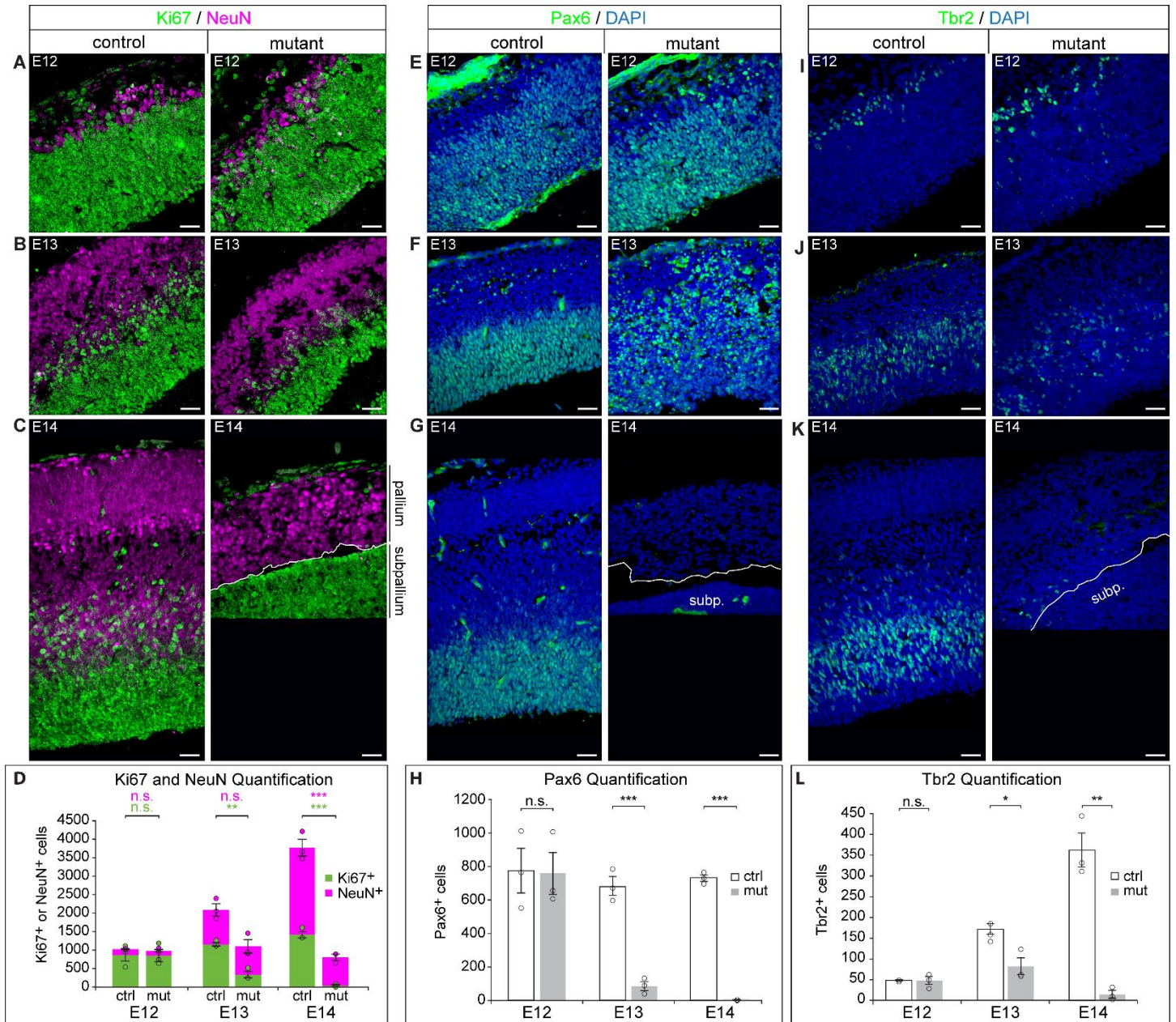
Figure 3. U11 loss results in depletion of RGCs. (**A-C**) IF for Ki67 (green) and NeuN (magenta) on sagittal sections of the control (left) and mutant (right) pallium across (**A**) E12, (**B**) E13, and (**C**) E14, with (**D**) quantification. (**E-G**) IF for Pax6 (green) on sagittal sections of the control (left) and mutant (right) pallium across (**E**) E12, (**F**) E13, and (**G**) E14, with (**H**) quantification. (**I-K**) IF for Tbr2 (green) on sagittal sections of the control (left) and mutant (right) pallium across (**I**) E12, (**J**) E13, and (**K**) E14, with (**L**) quantification. Scale bars=30 μm. Data are represented as mean±SEM. For details of statistical methods, see Table S8. Subp.=subpallium; n.s.=not significant; *=$P<0.05$; **=$P<0.01$; ***=$P<0.001$. See also Fig. S2.

A Expression of protein-coding genes

- Downregulated in mutant
- Upregulated in mutant
- Non-differentially expressed
- ○ MIG

B *Rnu11*

C *Spc24*

D E12 ctrl   E12 mut
CC3   γH2AX   DAPI

% of γH2AX⁺ cells
pyknotic γH2AX⁺ | CC3⁺& H2AX⁺

E E11 ctrl E11 mut E12 ctrl E12 mut
p53   γH2AX   DAPI

γH2AX
p53

F γH2AX DAPI
Pax6   Tbr2   NeuN

% of non-pyknotic γH2AX⁺ cells
Pax6⁺& γH2AX⁺ | Tbr2⁺& γH2AX⁺ | NeuN⁺& γH2AX⁺

G E12 mut
p53   Pax6   DAPI

Pax6⁻ / Pax6⁺ of p53⁺ cells
Pax6⁻ / Pax6⁺ of DAPI⁺ cells

Figure 4. U11 loss triggers DNA damage and p53 upregulation in RGCs. (**A**) Scatterplot depicting the expression of protein-coding genes ≥1 FPKM in the control (x-axis) and mutant (y-axis) E12 pallium. Inset shows the E12 mutant pallium, with dashed lines marking the dissected region. (**B-C**) Normalized expression, determined by qRT-PCR on E12 control and mutant pallium, for (**B**) *Rnu11* and (**C**) *Spc24*. (**D**) IF for CC3 (green) and γH2AX (magenta) in the E12 control (ctrl) and mutant (mut) pallium, with quantification. (**E**) IF for γH2AX (magenta) and p53 (green) in E11 and E12 ctrl and mut sagittal pallial sections, with quantification. Inset pie charts show the percentage of γH2AX$^+$ cells that upregulated p53 (p53$^+$) (left) and the percentage of p53$^+$ cells that were γH2AX$^+$ (right). (**F**) IF for γH2AX (magenta) and Pax6 (green), Tbr2 (green), or NeuN (green), on sagittal sections of the E12 mut pallium, with quantification. (**G**) IF for p53 (magenta) and Pax6 (green) in the E12 mut pallium, with pie charts showing the percentage of Pax6$^+$ cells of the p53$^+$ population (left) and of all DAPI$^+$ cells (right). Scale bars=30 µm. Quantification data are represented as mean±SEM. For details of statistical methods, see Table S8. n.s.=not significant; *=*P*<0.05; **=*P*<0.01; ***=*P*<0.001.
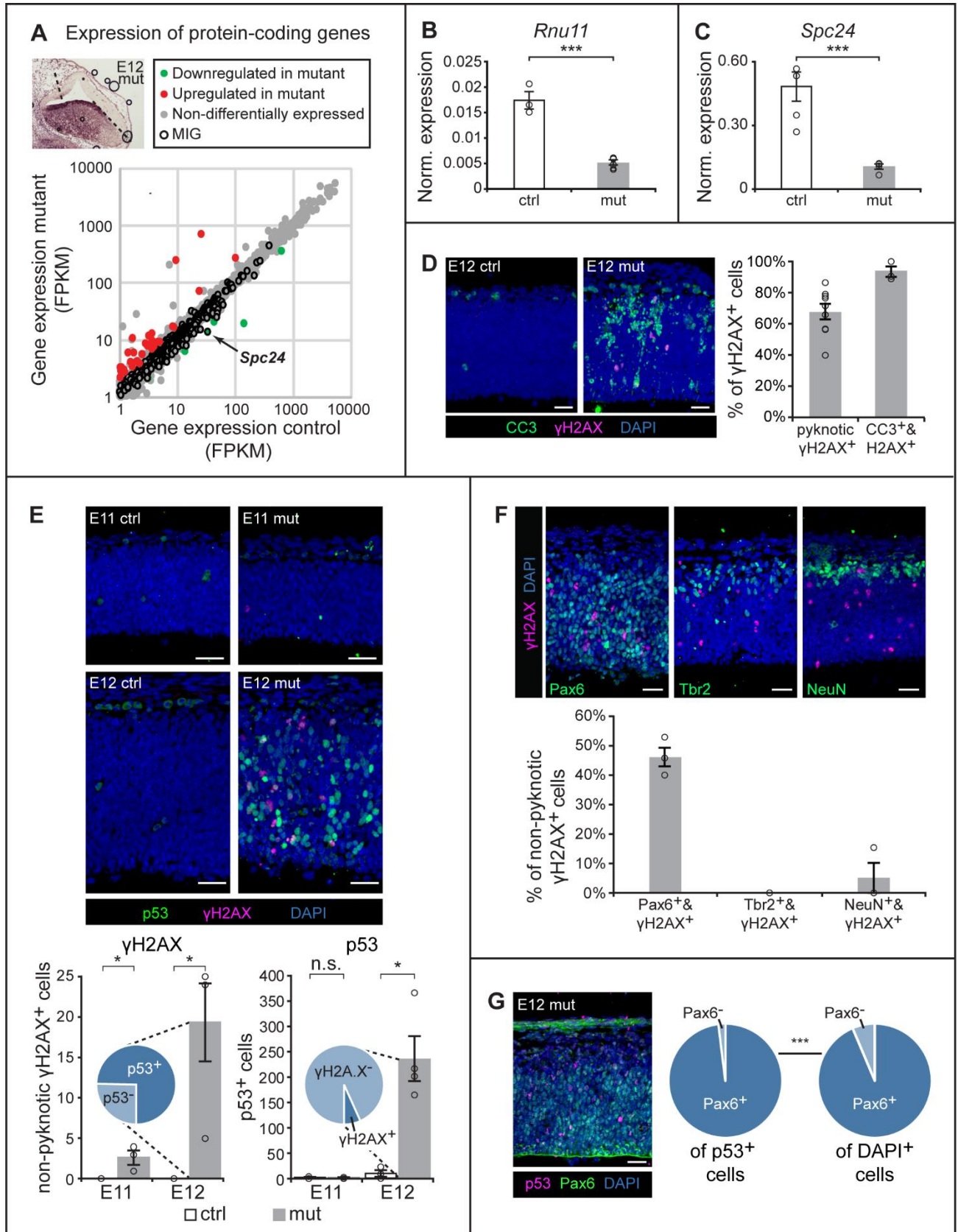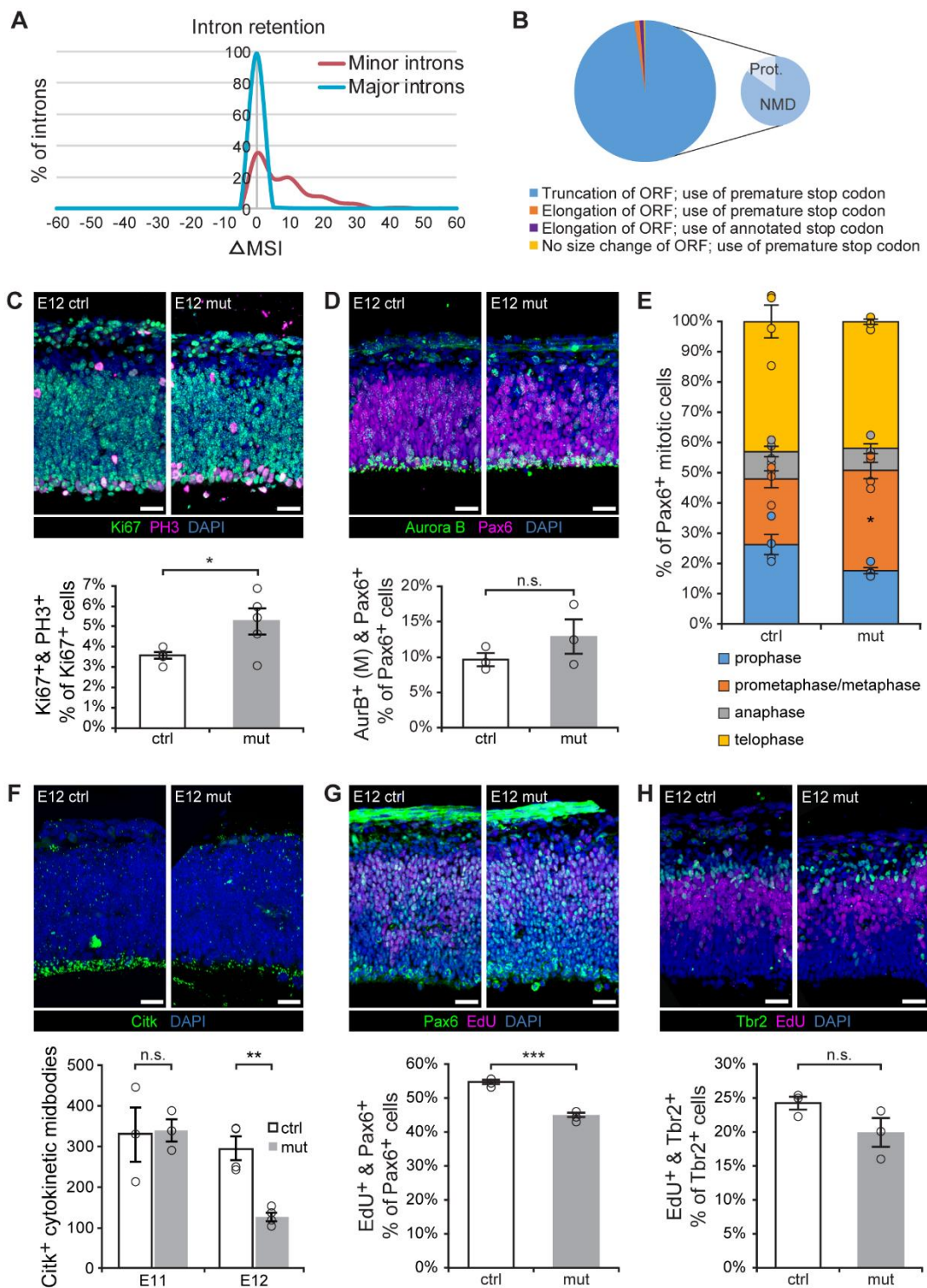
Figure 5. U11-null RGCs exhibit S-phase, metaphase, and cytokinesis defects. (**A**) Frequency plot of the change in mis-splicing index (ΔMSI, x-axis) of major (blue) and minor (red) introns. (**B**) Pie chart showing the effect of minor intron retention on the open reading frame (ORF), for the 186 minor introns with significantly

elevated retention, across all annotated MIG transcripts requiring minor intron splicing. The truncation category is further broken down into the percentage of transcripts predicted to be degraded by nonsense-mediated decay (NMD) or to produce protein (prot.). (**C**) IF for Ki67 (green) and PH3 (magenta) in sagittal sections of the E12 control and mutant pallium, with quantification. (**D**) IF for Aurora B (green, AurB) and Pax6 (magenta) in sagittal sections from E12 ctrl and mut pallium, with quantification of mitosis-specific Aurora B staining (M). (**E**) Quantification of the percentage of Aurora B$^+$ cells in different mitotic phases for E12 ctrl and mut pallium. (**F**) IF for Citk (green) in sagittal sections of ctrl and mut E12 pallium, quantification of Citk$^+$ cytokinetic midbodies along the ventricular edge in the E11 and E12 control and mutant pallium. (**G**) IF for Pax6 (green) and EdU (magenta) on E12 ctrl and mut sagittal pallial sections, with quantification. (**H**) IF for Tbr2 (green) and EdU (magenta) on sagittal sections of E12 ctrl and mut pallium, with quantification. Scale bars=30 µm. Data are represented as mean±SEM. For details of statistical methods, see Table S8. n.s.=not significant, *=P<0.05, **=P<0.01, ***=P<0.001. See also Fig. S3 and S4, and Tables S3 and S4.

A

E12 mut

γH2AX EdU
DAPI

of non-pyk.
γH2AX⁺ cells — n.s. — of DAPI⁺ cells

EdU⁺ / EdU⁻

B

E12 mut

p53 EdU
DAPI

of p53⁺ cells — *** — of DAPI⁺ cells

EdU⁺ / EdU⁻

C

E12 mut

AuroraB p53
DAPI

G2

of p53⁺ cells — *** — of DAPI⁺ cells

AurB⁺ / AurB⁻

M

of p53⁺ cells — *** — of DAPI⁺ cells

AurB⁺ / AurB⁻

D

E12 mut

CC3 EdU
TUNEL DAPI

of non-pyk.
CC3⁺ cells — n.s. — of DAPI⁺ cells

EdU⁺ / EdU⁻

E

E12 mut

CC3 AuroraB
TUNEL DAPI

% of non-pyk. CC3⁺ cells

7%
6%
5%
4%
3%
2%
1%
0%

AuroraB⁺&
non-pyk. CC3⁺
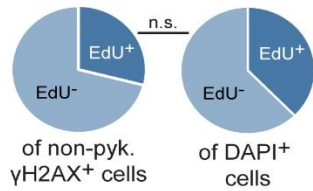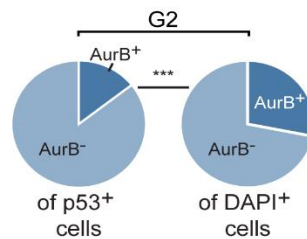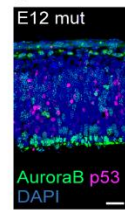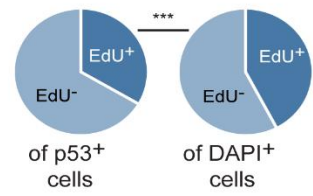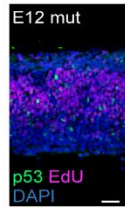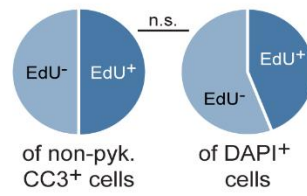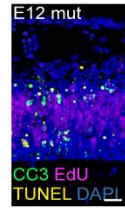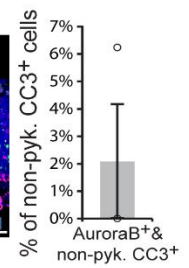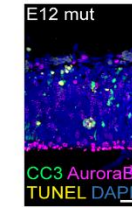
Figure 6. P53 upregulation and apoptosis predominantly occur in either cells in G1 or post-mitotic cells. (**A**) IF for γH2AX (green) and EdU (magenta) in sagittal sections of E12 mutant (mut) pallium, with pie charts showing the percentage of EdU$^+$ cells of the non-pyknotic (non-pyk.) γH2AX$^+$ and DAPI$^+$ populations. See also Fig. S5. (**B**) IF for p53 (green) and EdU (magenta) in sagittal sections of E12 mut pallium, with pie charts showing the percentage of EdU$^+$ cells of the p53$^+$ and DAPI$^+$ populations. (**C**) IF for Aurora B (green, AurB) and p53 (magenta) in sagittal section of the E12 mut pallium, with pie charts showing the percentage of G2 Aurora B$^+$ cells of the p53$^+$ and DAPI$^+$ populations (left), and the percentage of mitotic (M) Aurora B$^+$ cells of the p53$^+$ and DAPI$^+$ populations (right). (**D**) IF for CC3 (green), EdU (magenta), and TUNEL (yellow) in sagittal section of E12 mut pallium, with pie charts showing the percentage of EdU$^+$ cells of the non-pyknotic CC3$^+$ cell population. (**E**) IF for CC3 (green), Aurora B (magenta), and TUNEL (yellow) in sagittal sections of the E12 mut pallium, with quantification. Scale bars=30 µm. Quantification data are represented as mean±SEM. For details of statistical methods, see Table S8. n.s.=not significant, ***=P<0.001.
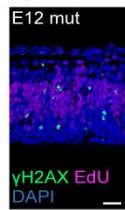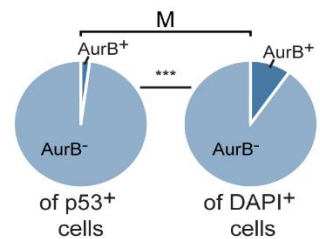
A

The effects of U11 loss on the different cell populations of the developing cortex

wild-type dorsal telencephalon

U11-null dorsal telencephalon

E12

E13

E14

Cell Types Legend

radial glial cell

= U11+ = U11−

intermediate progenitor cell

= U11+ = U11−

newly-born neuron

= U11+ = U11−

differentiating neuron

= U11+ = U11−

Nucleus Color Legend

● = dividing progenitor

○ = newly born NPC

● = apoptotic
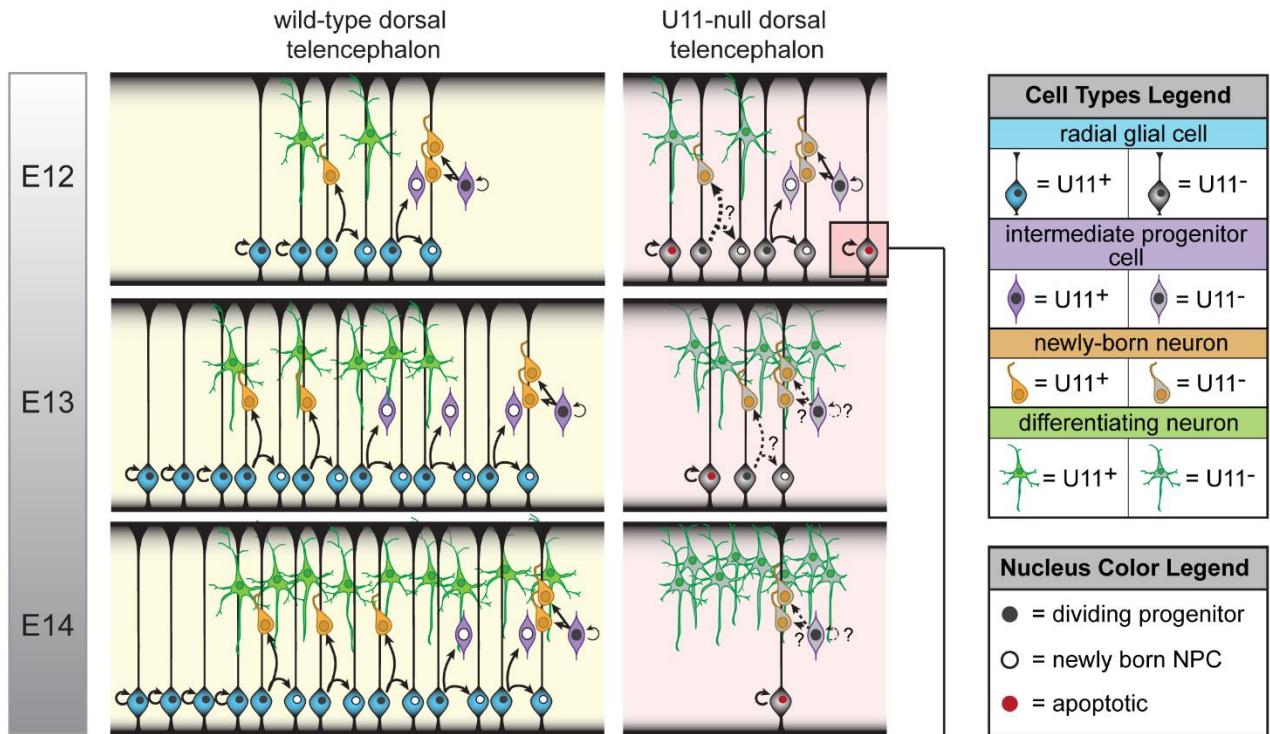
B

Cell cycle progression in U11-null, self-amplifying radial glial cells

cell death

p53 upreg.

DNA damage

U11 loss at G1

U11 loss at G2

Minor intron retention
- *Cdc45*
- *Dna2*
- *E2f6*
- *Prim1*
- *Rfc5*
- *Uba3*

Minor intron retention
- *Cep164*
- *Dctn3*
- *Dync1li1*
- *Gak*
- *Mau2*
- *Nedd1*
- *Zfp207*

Minor intron retention
- *Ahctf1*
- *Ccnt1*

prolonged

Citk mislocation?

cell death?

cell death

p53 upreg.

G1   S   G2   Pro.   Met.   Ana.   Tel.   Cyt.   G1

Mitosis/Cytokinesis

Cell Color Legend

Nucleus	Cell body	
○ = DNA damage		
○ = p53 upregulation	= U11+	= U11−
● = apoptotic		

Figure 7. Model of cortical development in U11 cKO mice. (**A**) Schematic representing cortical development in wild-type and mutant embryos, from E12 to E14. Black arrows show type of cell division; arrow thickness denotes relative frequency of that division. Question marks and dashed lines indicate events that remain to be explored. (**B**) Schematic of proliferating RGCs progressing through the cell cycle in the late E11/early E12 pallium. Arrow color denotes presence (blue) or absence (black) of U11. MIGs with significantly elevated minor intron retention, and with known functions at specific cell cycle phases, are listed in boxes. Pro.=prophase; met.=metaphase; ana.=anaphase; tel.=telophase; cyt.=cytokinesis. See also Table S5.

Supplemental Information

Supplemental Figures

Figure S1. Generation and confirmation of the *Rnu11* cKO mice. Related to Figure 1. (**A**) Schematic of the *Rnu11* locus. The gray box represents the predicted gene *Gm28874*. Below the *Rnu11* locus schematic is the targeting construct used to introduce the loxP sites by homologous recombination (dashed lines). (**B**) Schematic representing the targeted allele, showing the primers used to interrogate the 5' loxP site (black and green arrows, left) and the 3' loxP site (black and purple arrows, right). For the 5' loxP site primer set, the outermost forward primer (black arrow, left) was designed outside the 5' arm of homology, with the outermost reverse primer (black arrow, left) positioned downstream of the 5' loxP site. The inner set of nested primers (green arrows) were designed in the 5' arm of homology and within the 5' loxP site, respectively. For the 3' loxP site primer set, the outermost forward primer (black arrow, right) was designed in the Frt site located upstream of the 3' loxP site, with the outermost reverse primer (black arrow, right) positioned downstream of the 3' arm of homology. The inner set of nested primers (purple arrows) were designed in the 3' loxP site and the 3' arm of homology, respectively. (**C**) Agarose gel images of long-range nested PCRs, performed on genomic DNA (gDNA) from targeted ES cells, using the 5' loxP site primer set (black and green arrows, left) and the 3' loxP site primer set (black and purple arrows, right). The number at the right of each gel image represents the expected product size produced from this strategy.

Figure S2. U11 loss and death of self-amplifying RGCs in the mutant pallium. Related to Figure 3. (**A**) Separated channels for sagittal section U11 FISH (middle row) and immunofluorescence (IF) for Ki67 (green) and NeuN (magenta) (top row), with overlay (bottom row), from the E12 and E13 control (ctrl) and mutant (mut) pallium. Scale bars=30 µm. (**B**) IF for Pax6 (green) and cleaved caspase 3 (CC3, magenta) on sagittal section of E13 mutant pallium. White line marks the boundary between the subpallium and the pallium. Scale bar=30 µm. (**B'-B'''**) Magnified images of the dashed box in (**B**), showing overlay of all channels (**B'**), Pax6 and DAPI (**B''**), and CC3 and DAPI (**B'''**). Scale bars=7 µm. (**C**) IF for CC3 (magenta) and Tuj1 (green) in sagittal section of the E12 ctrl and mut pallium, with bar graphs showing the percentage of CC3$^+$ cells that were pyknotic (left) and the percentage of non-pyknotic CC3$^+$ cells that were Tuj1$^+$ (right). Scale bars=30 µm. (**D-E**) Bar graphs showing quantification of cells with nuclear Pax6 staining (**D**) or cells with nuclear Tbr2 staining (**E**) across development in the mutant pallium, from E12 and E14. Statistical significance across the three tested time-points was determined by one-way ANOVA, followed by Tukey's multiple comparison test to determine specific *P* values. (**F**) IF for BrdU (magenta) and NeuN (green) in the E13 ctrl and mut pallium, which had been pulsed with BrdU at E12. Scale bars=30 µm. At right are bar graphs showing the percentage of NeuN$^+$ cells that were BrdU$^+$ in the E13 pallium, or the percentage of non-pyknotic BrdU$^+$ cells that were NeuN$^+$ in the E13 pallium. Statistical significance was determined by two-tailed student's *t*-tests (Table S8). Quantification data are represented as mean±SEM from *N*=3 for each condition per time-point; individual data points are superimposed on bar graphs. Non-pyk.=non-pyknotic. n.s.=not significant; *=*P*<0.05; **=*P*<0.01.

A

Minor intron retention

B

DAVID analysis of MIGs with elevated minor intron retention

GO-term Functional Enrichment	Genes	Benjamini
nucleoplasm	41	9.405E-6
nucleotide binding	36	9.190E-4
protein transport	19	3.069E-3
cell cycle	18	9.714E-3
nuclear pore complex assembly	4	2.007E-2
poly(A) RNA binding	22	2.176E-2
centrosome	13	2.324E-2

Figure S3. Validation of expression and minor intron retention changes in the E12 mutant pallium. Related to Figure 5. (**A**) Minor intron retention of *Coa3* (left), *Parp1* (middle), and *Pten* (right) in the E12 ctrl and mut pallium, as determined by qRT-PCR. The value plotted is the average ratio of normalized unspliced expression/normalized spliced expression ± SEM from *N*=3 for each condition. Individual data points are superimposed on the bar graphs. Statistical significance was determined by two-tailed student's *t*-tests (Table S8). *=*P*<0.05, **=*P*<0.01, ***=*P*<0.001. (**B**) GO Terms enriched for by DAVID analysis of MIGs with statistically significant elevated minor intron retention in the E12 mutant pallium, with cell cycle-related terms highlighted in yellow.

Figure S4. Cell cycle defects are not observed in the E11 mutant pallium, in IPCs of the E12 mutant pallium, or in G2 phase. Related to Figure 5. (**A**) IF for Aurora B (green, AurB) showing phase-specific Aurora B staining patterns in cells in G2, prophase (pro.), prometaphase (prometa.), metaphase (meta.), anaphase (ana.), and telophase (telo.) in the E12 pallium. Scale bars=4 µm. (**B**) IF for Aurora B (green) and Tbr2 (magenta) in sagittal sections of control (ctrl) and mutant (mut) E12 pallium, with bar graph showing the percentage of Tbr2$^+$ cells with mitosis- and G2-specific (N=4) Aurora B staining patterns. (**C**) Bar graph showing the percentage of Aurora B$^+$/Tbr2$^+$ mitotic cells in prophase, prometaphase/metaphase (prometa./meta.), anaphase, and telophase (N=4). (**D**) IF for Citk (green) in sagittal sections of E11 control and mutant pallium. (**E**) IF for Pax6 (green) and EdU detection (magenta) in sagittal sections from E11 control (ctrl, left) and mutant (mut, right) pallium, with bar graph showing the percentage of Pax6$^+$ cells that were EdU$^+$ in the E11 ctrl and mut pallium. (**F**) IF for cyclin B1 (green) in sagittal sections of the E12 ctrl and mut pallium, with bar graph showing the number of cell with cytoplasmic (cytopl.) cyclin B1. (**G**) Bar graph showing the percentage of Pax6$^+$ cells with G2-specific Aurora B$^+$ staining in the E12 ctrl and mut pallium. Scale bars=30 µm, unless otherwise specified. Quantification data are represented as mean±SEM from N=3 for each condition per time-point, unless otherwise specified. Statistical significance was determined by two-tailed student's t-test (Table S8). n.s.=not significant.

Figure S5. Cells with DNA damage are not in mitosis. Related to Figure 6. IF for PH3 (green) and γH2AX (magenta) in a sagittal section of the E12 mutant pallium. Scale bar=30 µm.

Table S1. RNAseq gene expression data. Related to Figure 4. FC=expression fold-change between control and mutant.

Click here to Download Table S1

Table S2. Mammalian functions of the 4 genes upregulated in the mutant pallium that enriched for "intrinsic apoptotic signaling pathway in response to DNA damage by p53 mediator" by DAVID. Related to Figure 4. FC=expression fold-change between control and mutant. Ave=average.

Gene	Synonyms	Ave FPKM Ctrl	Ave FPKM Mut	FC	Function Description
Bbc3	*Puma, Jfy1, Jfy-1*	0.7199858	1.8057943	2.43627	p53 upregulated modulator of apoptosis, a BH3 domain-containing gene (PMID: 11572983); alongside Pmaip1 (below), important activator of genotoxic stress-induced apoptosis in NPCs (PMID: 16822983); required for apoptosis driven by increased p53 expression (PMID: 12574499)
Eda2r	*Xedar*	1.6703153	10.5807371	6.85729	both *EDA2R* and its ligand, *EDA*, are transcriptionally activated by p53 (PMID: 19543321, 20501644); regulator of p53-mediated apoptosis via interaction with the death receptor FAS, and increased expression of EDA2R results in upregulation/stabilization of FAS protein levels (PMID: 19543321)
Perp	*Kcp1, Krtcap1, Pigpc1, Thw*	0.4671268	1.0282991	2.23922	p53 apoptosis factor related to PMP-22; transcriptionally activated by p53 during p53-mediated apoptosis, but not during p53-mediated G1 arrest (PMID: 10733530, 14707288); induces p53 upregulation, post-translational p53 modifications that disrupt MDM2-p53 binding, and p53 nuclear translocation (PMID: 21451571); important positive regulator of p53-mediated apoptosis in the embryonic mouse brain (PMID: 14614825); DNA damage upregulates *Perp* expression (PMID: 14614825)
Pmaip1	*Noxa, Apr*	0.7210288	2.3228602	2.56006	pro-apoptotic, BH3 domain-containing gene whose transcription is activated by p53 (PMID: 10807576, 14500851); alongside Bbc3 (above), important activator of genotoxic stress-induced apoptosis in NPCs (PMID: 16822983)

Table S3. Minor intron retention data, derived from RNAseq data. Related to Figure 5. *P*-values were determined by two-tailed student's *t*-test. Rep=replicate; Avg=average. MSI=mis-splicing index.

Click here to Download Table S3

Table S4. Prediction of the effect of minor intron retention in the isoforms of MIGs with significant elevation of minor intron retention in the E12 mutant pallium. Related to Figure 5. ORF=open reading frame; NMD=nonsense-mediated decay.

Click here to Download Table S4

Table S5. Mammalian functions of the 21 MIGs regulating cell cycle with significantly elevated minor intron retention the mutant pallium. Related to Figures 5, S3, and S4. *P*-values were determined by two-tailed student's *t*-test. Syns=synonyms, ave=average. MSI=mis-splicing index.

Click here to Download Table S5

Table S6. The DNA damage response functions of 14 MIGs with significantly elevated minor intron retention in the mutant pallium. Related to Figure 4. MSI=mis-splicing index. *P*-values were determined by two-tailed student's *t*-test. Syns=synonyms, ave=average.

MIG	Syns	Ave FPKM Ctrl	Ave FPKM Mut	Ave MSI Ctrl	Ave MSI Mut	MSI *P*-value	ΔMSI	DNA Damage Response Function Description
Baz1b	*Wstf, Wbscr9, Wbscr10*	21.907384	25.945518	5.447441	12.41971	0.019728	13.97227	forms nucleosome remodeling complex with ISWI (complex: WICH), which phosphorylates and maintains this phosphorylation of H2AX (ɣH2AX), thereby regulating important steps in the DNA damage response process (PMID: 19092802)
Ccnk	*Cpr4, CycK*	55.348807	5.326979	5.053107	27.09289	0.004641	22.03978	cyclin K; when complexed with Cdk9, accumulates on chromatin in response to replication stress, and ssDNA in stressed cells (PMID: 20930849)
Cep164	*Nphp15*	5.060874	5.324126	5.904086	30.06079	0.000429	24.156701	centrosomal protein that is phosphorylated by the DNA damage response proteins ATR and ATM; siRNA-mediated knockdown in HeLa cells results in reduced phosphorylation of multiple DNA damage response proteins and chromosome missegregation (PMID: 18283122)
Cul1		41.697261	47.309440	2.804814	16.18051	0.001812	13.3757	as part of the SCF E3 ubiquitin ligase complex, ubiquitinates Ku80, a component of the initiating complex of the NHEJ double-strand break DNA repair pathway, thereby regulating this complex's removal from DNA (PMID: 23324393)
Cul4a		11.101313	12.071160	3.608965	15.74483	0.044297	12.13587	cullin; ubiquitin ligase that targets Ddb1 (another MIG, below) and Ddb2, both of which act to initiate the DNA damage response, for ubiquitination and degradation, thereby regulating the DNA damage response (PMID: 19481525)
Dna2	*Dna2l*	3.9216094	3.7578457	4.807850	17.42876	0.015044	12.62091	due to 5' to 3' endonuclease activity, involved in resection extension in homologous recombination-mediated DNA double stranded break repair (PMID: 28718810)

Ddb1	*XPE, DDBA, XAP1, XPCE*	86.093717	88.333331	0.461818	2.706198	0.004385	2.244381	large subunit of DNA damage-binding complex, which functions in nucleotide excision repair (PMID: 16951172); loss of *Ddb1* in mouse brain results in accumulation of cell cycle regulators and increased genomic instability, ultimately causing apoptosis of proliferating neuronal progenitors (PMID: 17129780)
E2f1	*Rbp3, Rbap1, Rbbp3*	6.067779	6.486815	12.91249	53.23981	0.000964	40.32732	upregulated in response to DNA damage, and promotes DNA damage-induced apoptosis (PMID: 11459832); indirectly regulates the transcription of the DNA damage response gene *GADD45A* (PMID: 20713352)
Ercc5	*Xpg*	5.363914	6.275879	1.333767	7.642992	0.048076	6.309225	single strand-specific DNA endonuclease involved in the 3' incision step of nucleotide excision repair (PMID: 7657672)
Exo1	*Msa, Hex1*	4.4268470	4.1420745	3.731127	9.386061	0.008405	5.654934	5' to 3' endonuclease involved in DNA mismatch repair and resection extension in homologous recombination-mediated DNA double stranded break repair (PMID: 24705021)
Ints7		8.821004	8.814813	3.590800	13.52046	0.012655	9.929663	recruited to sites of DNA damage and interacts with SSB1, a DNA damage sensor recognized by ATM (PMID: 21659603)
Parp1	*Parp, Ppol, Adprt, Artd1, Adprt1*	47.879274	47.679811	0.771961	14.72329	0.002560	13.95133	nuclear protein that promotes formation of poly(ADP-ribose) chains (PARylation), which transfers ADP-ribose group from NAD+ to target protein and forms a scaffold around DNA breaks, allowing for recruitment of essential DNA damage response factors (PMID: 21989215, 22431722)
Usp10	*UBPO, Uchrp*	10.625277	8.050707	4.474797	17.26511	0.012563	12.79031	after DNA damage, phosphorylated by ATM, resulting in Usp10 stabilization and transport to the nucleus, where it deubiquitylates p53, thereby stabilizing p53 (PMID: 20096447)

Table S7. Primer sequences for RT-PCR.

Primer Name	Primer Direction	Sequence (5' to 3')
Rnu11 cKO, 5' loxP	Forward (primer 1)	ACCCTCCCCTACTGTTTTAC
	Reverse (primer 2)	AGGCTGCTACAGGATGACTC
Rnu11 cKO, 3' loxP	Forward (primer 3)	CATGTGTTTGCTGGGAATTG
	Reverse (primer 4)	CTCATGAGGCAGATCTCTGAA
Hist1h1a expression	Forward	AGAAGAACAACAGCCGCATCAAACTGG
	Reverse	CTTGGACTCAGCCTTCTTGTTCAGCTT
Cre genotyping	Forward	TATCCAGCAACATTTGGGCCAGCT
	Reverse	AACATTCTCCCACCGTCAGTACGTGA
Emx1-Cre zygosity, wild-type	Forward	AAGGTGTGGTTCCAGAATCG
	Reverse	CTCTCCACCAGAAGGCTGAG
Emx1-Cre zygosity, mutant	Forward	GATCTCCGGTATTGAAACTCCAGC
	Reverse	GCTAAACATGCTTCATCGTCGG
U11 expression	Forward	AAAGGGCTTCTGTCGTGAGTGGC
	Reverse	CCGGGACCAACGATCACCAG
Neat1 expression	Forward	AATTGGCCAGAAGACAACAGGGTTTGC
	Reverse	GTATTCAGTGGCAAAGCACTCATGAGG
Coa3 minor intron splicing	Forward	CAGTTGCAGTTTATGCGGCAGGTG
	Reverse (intronic)	CTAGCCACCCTTGCTGTTTTCCCAAA
	Reverse (exonic)	CAGCTTTGGCTTCATCTTCCAGCTC
Pten minor intron splicing	Forward	CTCCCAGACATGACAGCCATCATCAA
	Reverse (intronic)	CTACTCCCACGTTATCAGAGTGACAGAA
	Reverse (exonic)	CAAGTCTTTCTGCAGGAAATCCCATAGC
Parp1 minor intron splicing	Forward	AAAACCACCCCTGACCCTTCG
	Reverse (intronic)	GCACACAGCATAGCCAAGAAAGG
	Reverse (exonic)	AATGTACCTGGGGAGGGCAGTT
Sfrs10 expression	Forward	AGCAGGTCTTACAGCCGAGATTATCG
	Reverse	CCAAACACGCCAAGACAACAGTTG
Spc24 expression	Forward	CTCATACCTTGCACAGAACTGGGGTT
	Reverse	AATAAAAAGAAGCTGCAGGCCAGCC
Intergenic primers	Forward	GGATAGTTCATCTCCTGCAGGTCACAAG
	Reverse	GTCCCACCCATCTAGTTTAGCATCAGC

Table S8. Summary of statistical analyses performed.

Fig.	Experimental Paradigm (ex: immuno-staining)	*N*-value	*P*-value	t/f-value	Statistical test	Test for multiple testing?	Does data meet assumption of normality?
1B	qPCR	WT=3 WT/KO=3	6.43E-05	17.38388	Student's t-test [1]	No	Yes
1C	Genotype frequency	WT=20 Het=45 Mut=0	0.0001067	N/A	Chi-squared goodness of fit test	No	Yes
1J	Pallium thickness	Ctrl=3 Mut=3	0.63251 (E12) 0.96958 (E13) 0.02533 (E14)	-0.5168 (E12) 0.0405 (E13) 3.4805 (E14)	Student's t-test [1]	No	Yes

2A	TUNEL	Ctrl=3 Mut=3	0.587853	-0.58845	Student's t-test [1]	No	Yes
2B	TUNEL	Ctrl=4 Mut=4	0.000364	-7.19759	Student's t-test [1]	No	Yes
2C	TUNEL	Ctrl=3 Mut=3	0.001647	-7.55204	Student's t-test [1]	No	Yes
2D	TUNEL	Ctrl=4 Mut=4	0.017318	-3.25681	Student's t-test [1]	No	Yes
2E	CC3	Ctrl=3 Mut=3	0.348641	-1.06066	Student's t-test [1]	No	Yes
2F	CC3	Ctrl=4 Mut=4	0.006263	-4.11334	Student's t-test [1]	No	Yes
3D	Ki67	Ctrl=3 Mut=3	0.94384 (E12) 0.00114 (E13) 9.86E-05 (E14)	0.07497 (E12) 8.31546 (E13) 15.6004 (E14)	Student's t-test [1]	No	Yes
3D	NeuN	Ctrl=3 Mut=3	0.58591 (E12) 0.50374 (E13) 0.00256 (E14)	0.59165(E12) 0.73383 (E13) 6.71922 (E14)	Student's t-test [1]	No	Yes
3H	Pax6	Ctrl=3 Mut=3	0.91943 (E12) 0.00063 (E13) 2.83E-06 (E14)	0.1076 (E12) 9.6834 (E13) 38.116 (E14)	Student's t-test [1]	No	Yes
3L	Tbr2	Ctrl=3 Mut=3	0.983274 (E12) 0.030437 (E13) 0.001203 (E14)	-0.0223 (E12) 3.2822 (E13) 8.2035 (E14)	Student's t-test [1]	No	Yes
4B	qRT-PCR	Ctrl=4 Mut=4	0.000109	8.944523	Student's t-test [1]	No	Yes
4C	qRT-PCR	Ctrl=4 Mut=4	0.004161	4.487097	Student's t-test [1]	No	Yes
4E	yH2AX	Ctrl=3 Mut=3 (E11) Ctrl=3 Mut=4 (E12)	0.039021 (E11) 0.027471 (E12)	-3.02372 (E11) -4.02969 (E12)	Student's t-test [1] (E11) T-test: two sample assuming unequal variances (E12)	No	Yes
4E	P53	Ctrl=3 Mut=3 (E11) Ctrl=3 Mut=4 (E12)	0.57902 (E11) 0.01497 (E12)	0.60302 (E11) -5.05123 (E12)	Student's t-test [1] (E11) T-test: two sample assuming unequal variances (E12)	No	Yes
4G	Pax6/ p53	Mut=3	P<0.001 (Fisher's method) 0.1651 (N=1) 2.53E-04	N/A	Fisher Exact test[2]	No	Yes

			(N=2) 6.72E-04 (N=3)				
5C	Ki67/ PH3	Ctrl=5 Mut=5	0.036877	-2.50113	Student's t-test [1]	No	Yes
5D	Pax6/ AuroraB (M)	Ctrl=3 Mut=3	0.281507	-1.24374	Student's t-test [1]	No	Yes
5E	Pax6/ AuroraB	Ctrl=4 Mut=4	0.050205 (prophase) 0.022396 (prometaphase/ metaphase) 0.399731 (anaphase) 0.853745 (telophase)	2.443901 (prophase) -3.05402 (prometaphase/ metaphase) 0.906253 (anaphase) 0.19244 (telophase)	Student's t-test [1]	No	Yes
5F	Citk	Ctrl=3 Mut=3 (E11) Ctrl=4 Mut=4 (E12)	0.909922 (E11) 0.001502 (E12)	-0.1205 (E11) 5.5091 (E12)	Student's t-test [1]	No	Yes
5G	Pax6/ EdU	Ctrl=3 Mut=4	0.00013	10.58504	T-test: two sample assuming unequal variances	No	Yes
5H	Tbr2/ EdU	Ctrl=3 Mut=3	0.143103	1.972462	Student's t-test [1]	No	Yes
6A	yH2AX/ EdU	Mut=3	0.5<P<0.6 (Fisher's method) 0.0953 (n=1) 0.762 (n=2) 1.0 (n=3)	N/A	Fisher Exact test[2]	No	Yes
6B	P53/EdU	Mut=3	P<0.001 (Fisher's method) 0.0095 (N=1) 0.4087 (N=2) 4.61E-06 (N=3)	N/A	Fisher Exact test[2]	No	Yes
6C	P53/ AuroraB (M)	Mut=4	P<0.001 (Fisher's method) 3.94E-06 (N=1) 3.24E-04 (N=2) 0.0135 (N=3) 0.0115 (N=4)	N/A	Fisher Exact test[2]	No	Yes
6C	P53/ AuroraB (G2)	Mut=4	P<0.001 (Fisher's method) 9.18E-05	N/A	Fisher Exact test[2]	No	Yes

			(N=1) 2.76E-06 (N=2) 0.0321 (N=3) 2.01E-07 (N=4)				
6D	EdU/CC3	Mut=3	0.4<P<0.5 (Fisher's method) 0.345 (N=1) 0.586 (N=2) 0.265 (N=3)	N/A	Fisher Exact test[2]	No	Yes
S2C	CC3/pyknotic cells	Ctrl=3 Mut=3	0.001891	-7.28116	Student's t-test [1]	No	Yes
S2C	CC3/Tuj1	Ctrl=3 Mut=3	0.140357	-1.83533	Student's t-test [1]	No	Yes
S2D	Pax6	E12=3 E13=3 E14=3	0.001 (ANOVA) 0.002 (E12-E13) 0.719py (E13-E14)	30.835 (ANOVA)	One–way ANOVA	Post-hoc Tukey	Yes
S2E	Tbr2	E12=3 E13=3 E14=3	0.046 (ANOVA) 0.284 (E12-E13) 0.039 (E13-E14)	5.351 (ANOVA)	One–way ANOVA	Post-hoc Tukey	Yes
S2F	BrdU/ NeuN	Ctrl=3 Mut=3	0.0115 (%NeuN) 0.96281 (%BrdU)	4.416383 (%NeuN) 0.049606 (%BrdU)	Student's t-test [1]	No	Yes
S3A	qRT-PCR	Ctrl=3 Mut=3	0.009763 (Coa3) 0.014807 (Pten) 2.13E-06 (Parp1)	-4.6360 (Coa3) -4.1038 (Pten) -40.90389 (Parp1)	Student's t-test [1]	No	Yes
S4B	Tbr2/ AuroraB	Ctrl=4 Mut=4 (G2) Ctrl=3 Mut=3 (M)	0.544268 (G2) 0.890293 (M)	0.642447 (G2) -0.14693 (M)	Student's t-test [1]	No	Yes
S4C	Tbr2/ AuroraB	Ctrl=4 Mut=4	0.109109 (prophase) 0.640059 (prometaphase/ metaphase) 0.266296 (anaphase) 0.258209 (telophase)	-1.8803 (prophase) 0.492213 (prometaphase/ metaphase) 1.225527 (anaphase) 1.248928 (telophase)	Student's t-test [1]	No	Yes
S4E	Pax6/ EdU	Ctrl=3 Mut=3	0.114046	-2.01577	Student's t-test [1]	No	Yes
S4F	Cyclin B1	Ctrl=3	0.196738	1.547139	Student's	No	Yes

		Mut=3			t-test [1]		
S4G	Pax6/ AuroraB (G2)	Ctrl=3 Mut=3	0.223782	1.438129	Student's t-test [1]	No	Yes

[1] Two-sample t-test assuming equal variances

[2] Followed by Fisher's method to combine *P*-values

Supplemental Information
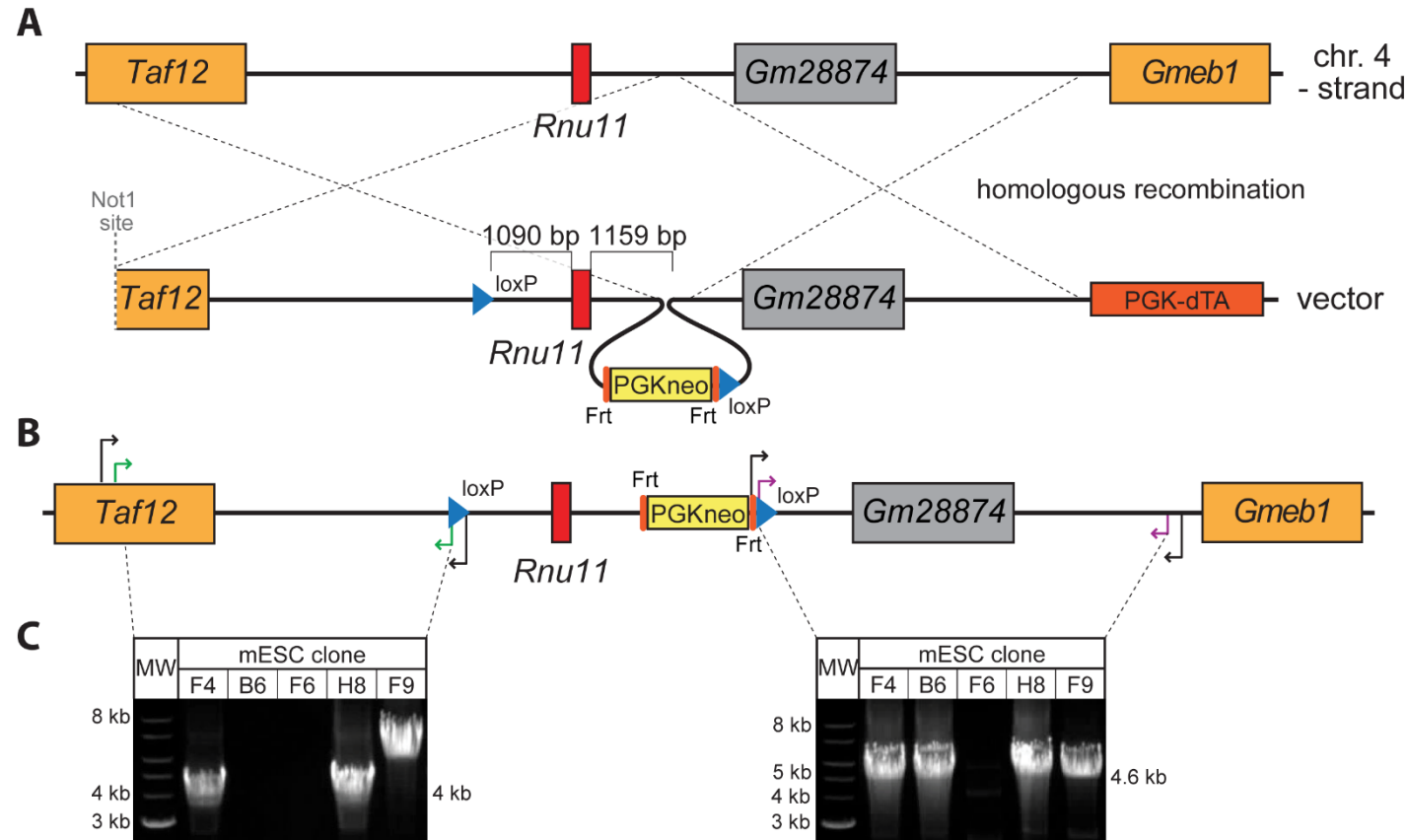
Supplemental Figures

Figure S1. Generation and confirmation of the *Rnu11* cKO mice. Related to Figure 1. (A) Schematic of the *Rnu11* locus. The gray box represents the predicted gene *Gm28874*. Below the *Rnu11* locus schematic is the targeting construct used to introduce the loxP sites by homologous recombination (dashed lines). **(B)** Schematic representing the targeted allele, showing the primers used to interrogate the 5' loxP site (black and green arrows, left) and the 3' loxP site (black and purple arrows, right). For the 5' loxP site primer set, the outermost forward primer (black arrow, left) was designed outside the 5' arm of homology, with the outermost reverse primer (black arrow, left) positioned downstream of the 5' loxP site. The inner set of nested primers (green arrows) were designed in the 5' arm of homology and within the 5' loxP site, respectively. For the 3' loxP site primer set, the outermost forward primer (black arrow, right) was designed in the Frt site located upstream of the 3' loxP site, with the outermost reverse primer (black arrow, right) positioned downstream of the 3' arm of homology. The inner set of nested primers (purple arrows) were designed in the 3' loxP site and the 3' arm of homology, respectively. **(C)** Agarose gel images of long-range nested PCRs, performed on genomic DNA (gDNA) from targeted ES cells, using the 5' loxP site primer set (black and green arrows, left) and the 3' loxP site primer set (black and purple arrows, right). The number at the right of each gel image represents the expected product size produced from this strategy.
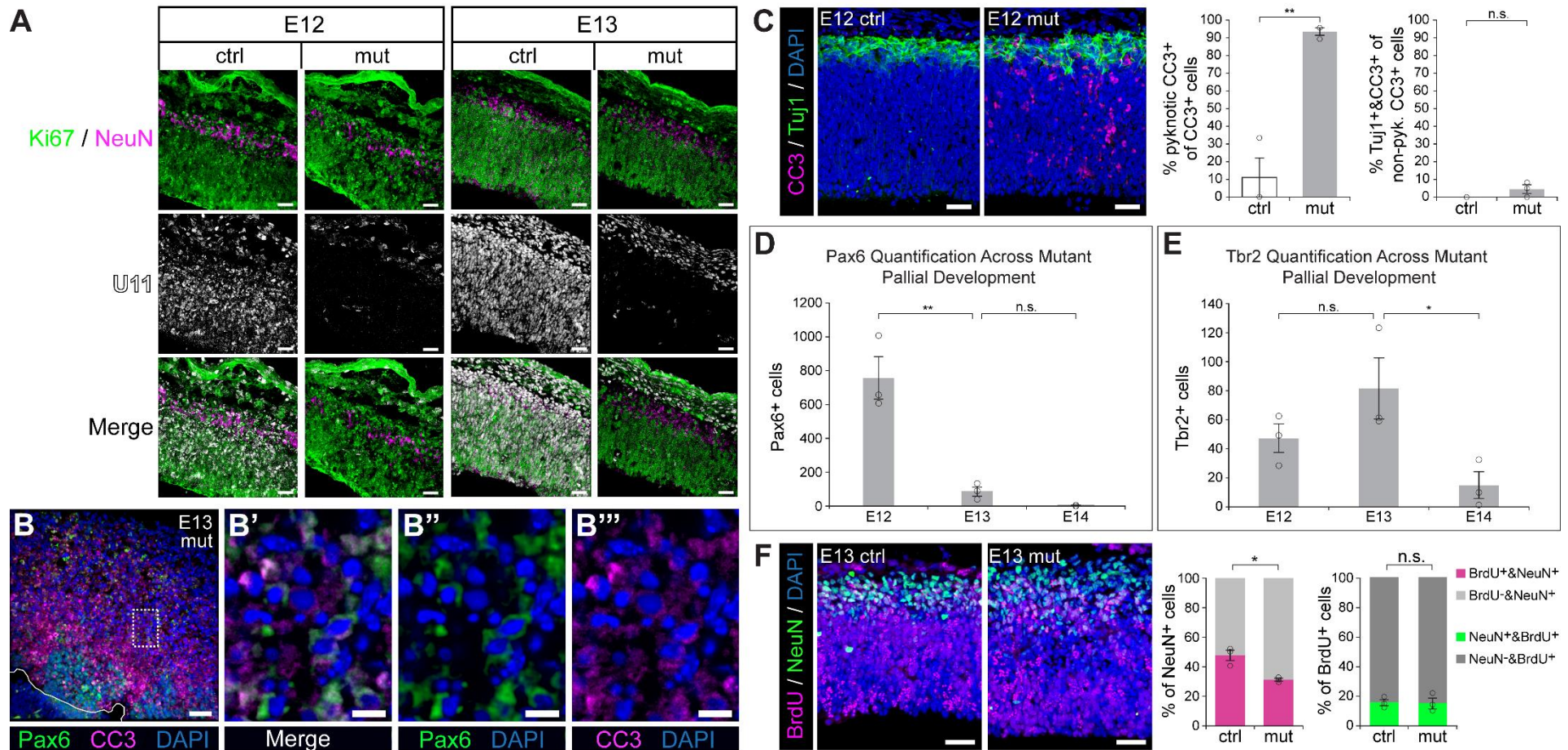
Figure S2. U11 loss and death of self-amplifying RGCs in the mutant pallium. Related to Figure 3. (**A**) Separated channels for sagittal section U11 FISH (middle row) and immunofluorescence (IF) for Ki67 (green) and NeuN (magenta) (top row), with overlay (bottom row), from the E12 and E13 control (ctrl) and mutant (mut) pallium. Scale bars=30 µm. (**B**) IF for Pax6 (green) and cleaved caspase 3 (CC3, magenta) on sagittal section of E13 mutant pallium. White line marks the boundary between the subpallium and the pallium. Scale bar=30 µm. (**B'-B'''**) Magnified images of the dashed box in (**B**), showing overlay of all channels (**B'**), Pax6 and DAPI (**B''**), and CC3 and DAPI (**B'''**). Scale bars=7 µm. (**C**) IF for CC3 (magenta) and Tuj1 (green) in sagittal section of the E12 ctrl and mut pallium, with bar graphs showing the percentage of CC3$^+$ cells that were pyknotic (left) and the percentage of non-pyknotic CC3$^+$ cells that were Tuj1$^+$ (right). Scale bars=30 µm. (**D-E**) Bar graphs showing quantification of cells with nuclear Pax6 staining (**D**) or cells with nuclear Tbr2 staining (**E**) across development in the mutant pallium, from E12 and E14. Statistical significance across the three tested time-points was determined by one-way ANOVA, followed by Tukey's multiple comparison test to determine specific P values. (**F**) IF for BrdU (magenta) and NeuN (green) in the E13 ctrl and mut pallium, which had been pulsed with BrdU at E12. Scale bars=30 µm. At right are bar graphs showing the percentage of NeuN$^+$ cells that were BrdU$^+$ in the E13 pallium, or the percentage of non-pyknotic BrdU$^+$ cells that were NeuN$^+$ in the E13 pallium. Statistical significance was determined by two-tailed student's t-tests (Table S8). Quantification data are represented as mean±SEM from N=3 for each condition per time-point; individual data points are superimposed on bar graphs. Non-pyk.=non-pyknotic. n.s.=not significant; *=$P<0.05$; **=$P<0.01$.

A

Minor intron retention

Coa3 (left), *Parp1* (middle), *Pten* (right)

B

DAVID analysis of MIGs with elevated minor intron retention

GO-term Functional Enrichment	Genes	Benjamini
nucleoplasm	41	9.405E-6
nucleotide binding	36	9.190E-4
protein transport	19	3.069E-3
cell cycle	18	9.714E-3
nuclear pore complex assembly	4	2.007E-2
poly(A) RNA binding	22	2.176E-2
centrosome	13	2.324E-2

Figure S3. Validation of expression and minor intron retention changes in the E12 mutant pallium. Related to Figure 5. (**A**) Minor intron retention of *Coa3* (left), *Parp1* (middle), and *Pten* (right) in the E12 ctrl and mut pallium, as determined by qRT-PCR. The value plotted is the average ratio of normalized unspliced expression/normalized spliced expression ± SEM from *N*=3 for each condition. Individual data points are superimposed on the bar graphs. Statistical significance was determined by two-tailed student's *t*-tests (Table S8). *=*P*<0.05, **=*P*<0.01, ***=*P*<0.001. (**B**) GO Terms enriched for by DAVID analysis of MIGs with statistically significant elevated minor intron retention in the E12 mutant pallium, with cell cycle-related terms highlighted in yellow.

Figure S4. Cell cycle defects are not observed in the E11 mutant pallium, in IPCs of the E12 mutant pallium, or in G2 phase. Related to Figure 5. (**A**) IF for Aurora B (green, AurB) showing phase-specific Aurora B staining patterns in cells in G2, prophase (pro.), prometaphase (prometa.), me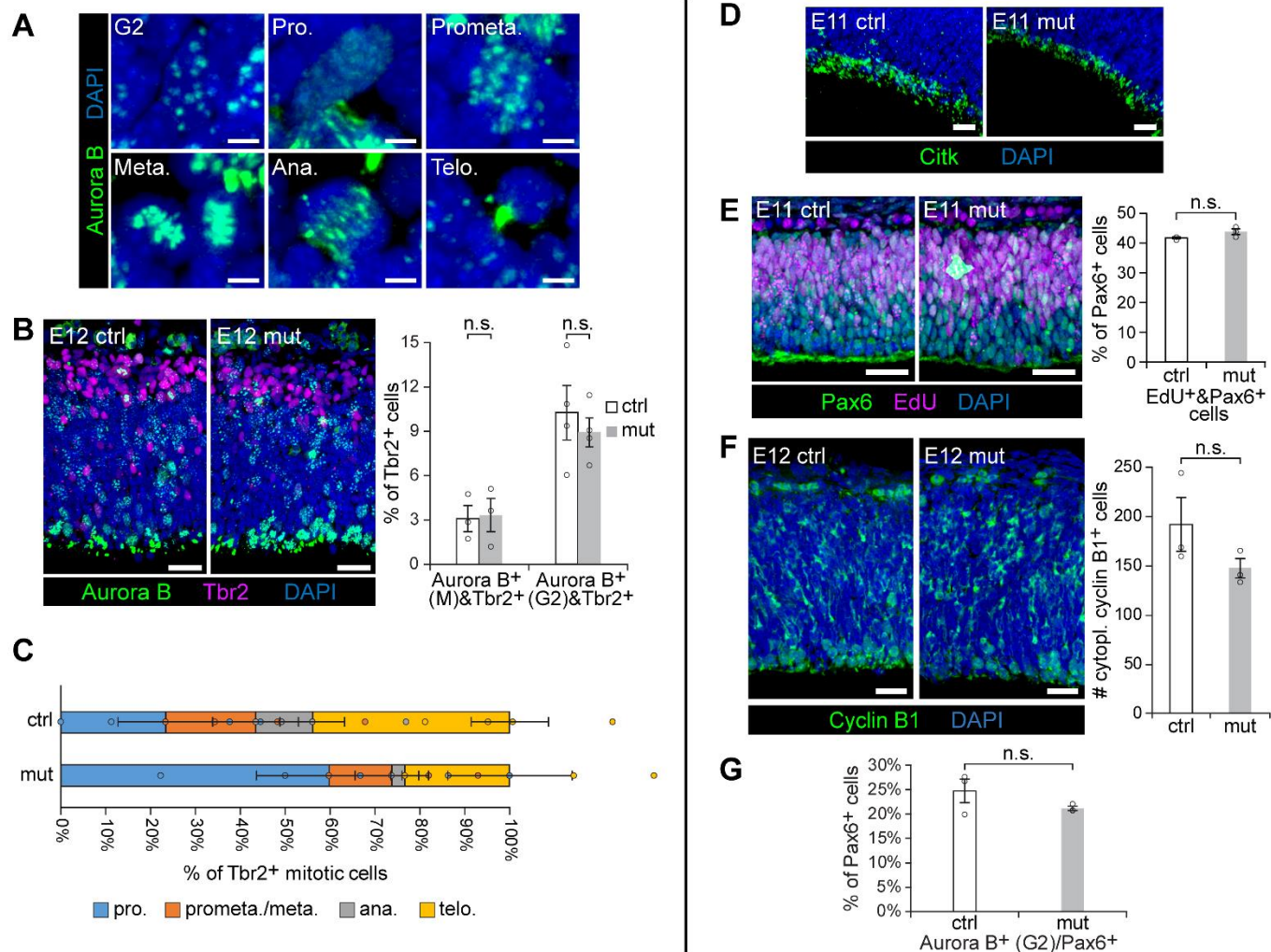taphase (meta.), anaphase (ana.), and telophase (telo.) in the E12 pallium. Scale bars=4 µm. (**B**) IF for Aurora B (green) and Tbr2 (magenta) in sagittal sections of control (ctrl) and mutant (mut) E12 pallium, with bar graph showing the percentage of Tbr2$^+$ cells with mitosis- and G2-specific (N=4) Aurora B staining patterns. (**C**) Bar graph showing the percentage of Aurora B$^+$/Tbr2$^+$ mitotic cells in prophase, prometaphase/metaphase (prometa./meta.), anaphase, and telophase (N=4). (**D**) IF for Citk (green) in sagittal sections of E11 control and mutant pallium. (**E**) IF for Pax6 (green) and EdU detection (magenta) in sagittal sections from E11 control (ctrl, left) and mutant (mut, right) pallium, with bar graph showing the percentage of Pax6$^+$ cells that were EdU$^+$ in the E11 ctrl and mut pallium. (**F**) IF for cyclin B1 (green) in sagittal sections of the E12 ctrl and mut pallium, with bar graph showing the number of cell with cytoplasmic (cytopl.) cyclin B1. (**G**) Bar graph showing the percentage of Pax6$^+$ cells with G2-specific Aurora B$^+$ staining in the E12 ctrl and mut pallium. Scale bars=30 µm, unless otherwise specified. Quantification data are represented as mean±SEM from N=3 for each condition per time-point, unless otherwise specified. Statistical significance was determined by two-tailed student's t-test (Table S8). n.s.=not significant.
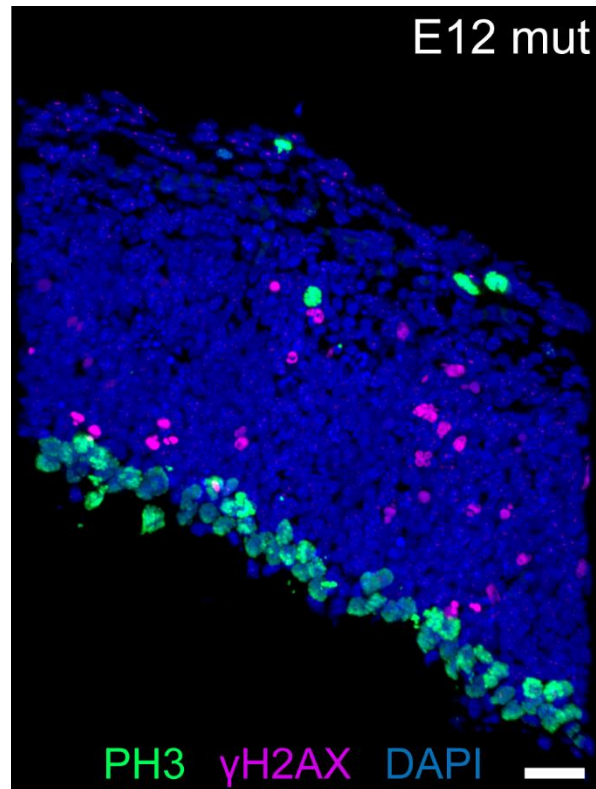
Figure S5. Cells with DNA damage are not in mitosis. Related to Figure 6. IF for PH3 (green) and γH2AX (magenta) in a sagittal section of the E12 mutant pallium. Scale bar=30 µm.

Table S1. RNAseq gene expression data. Related to Figure 4. FC=expression fold-change between control and mutant.

Click here to Download Table S1

Table S2. Mammalian functions of the 4 genes upregulated in the mutant pallium that enriched for "intrinsic apoptotic signaling pathway in response to DNA damage by p53 mediator" by DAVID. Related to Figure 4. FC=expression fold-change between control and mutant. Ave=average.

Gene	Synonyms	Ave FPKM Ctrl	Ave FPKM Mut	FC	Function Description
Bbc3	*Puma, Jfy1, Jfy-1*	0.7199858	1.8057943	2.43627	p53 upregulated modulator of apoptosis, a BH3 domain-containing gene (PMID: 11572983); alongside Pmaip1 (below), important activator of genotoxic stress-induced apoptosis in NPCs (PMID: 16822983); required for apoptosis driven by increased p53 expression (PMID: 12574499)
Eda2r	*Xedar*	1.6703153	10.5807371	6.85729	both *EDA2R* and its ligand, *EDA*, are transcriptionally activated by p53 (PMID: 19543321, 20501644); regulator of p53-mediated apoptosis via interaction with the death receptor FAS, and increased expression of EDA2R results in upregulation/stabilization of FAS protein levels (PMID: 19543321)
Perp	*Kcp1, Krtcap1, Pigpc1, Thw*	0.4671268	1.0282991	2.23922	p53 apoptosis factor related to PMP-22; transcriptionally activated by p53 during p53-mediated apoptosis, but not during p53-mediated G1 arrest (PMID: 10733530, 14707288); induces p53 upregulation, post-translational p53 modifications that disrupt MDM2-p53 binding, and p53 nuclear translocation (PMID: 21451571); important positive regulator of p53-mediated apoptosis in the embryonic mouse brain (PMID: 14614825); DNA damage upregulates *Perp* expression (PMID: 14614825)
Pmaip1	*Noxa, Apr*	0.7210288	2.3228602	2.56006	pro-apoptotic, BH3 domain-containing gene whose transcription is activated by p53 (PMID: 10807576, 14500851); alongside Bbc3 (above), important activator of genotoxic stress-induced apoptosis in NPCs (PMID: 16822983)

Table S3. Minor intron retention data, derived from RNAseq data. Related to Figure 5. *P*-values were determined by two-tailed student's *t*-test. Rep=replicate; Avg=average. MSI=mis-splicing index.

Click here to Download Table S3

Table S4. Prediction of the effect of minor intron retention in the isoforms of MIGs with significant elevation of minor intron retention in the E12 mutant pallium. Related to Figure 5. ORF=open reading frame; NMD=nonsense-mediated decay.

Click here to Download Table S4

Table S5. Mammalian functions of the 21 MIGs regulating cell cycle with significantly elevated minor intron retention the mutant pallium. Related to Figures 5, S3, and S4. *P*-values were determined by two-tailed student's *t*-test. Syns=synonyms, ave=average. MSI=mis-splicing index.

Click here to Download Table S5

Table S6. The DNA damage response functions of 14 MIGs with significantly elevated minor intron retention in the mutant pallium. Related to Figure 4. MSI=mis-splicing index. *P*-values were determined by two-tailed student's *t*-test. Syns=synonyms, ave=average.

MIG	Syns	Ave FPKM Ctrl	Ave FPKM Mut	Ave MSI Ctrl	Ave MSI Mut	MSI *P*-value	ΔMSI	DNA Damage Response Function Description
Baz1b	*Wstf, Wbscr9, Wbscr10*	21.907384	25.945518	5.447441	12.41971	0.019728	13.97227	forms nucleosome remodeling complex with ISWI (complex: WICH), which phosphorylates and maintains this phosphorylation of H2AX (ɣH2AX), thereby regulating important steps in the DNA damage response process (PMID: 19092802)
Ccnk	*Cpr4, CycK*	55.348807	5.326979	5.053107	27.09289	0.004641	22.03978	cyclin K; when complexed with Cdk9, accumulates on chromatin in response to replication stress, and ssDNA in stressed cells (PMID: 20930849)
Cep164	*Nphp15*	5.060874	5.324126	5.904086	30.06079	0.000429	24.156701	centrosomal protein that is phosphorylated by the DNA damage response proteins ATR and ATM; siRNA-mediated knockdown in HeLa cells results in reduced phosphorylation of multiple DNA damage response proteins and chromosome missegregation (PMID: 18283122)
Cul1		41.697261	47.309440	2.804814	16.18051	0.001812	13.3757	as part of the SCF E3 ubiquitin ligase complex, ubiquitinates Ku80, a component of the initiating complex of the NHEJ double-strand break DNA repair pathway, thereby regulating this complex's removal from DNA (PMID: 23324393)
Cul4a		11.101313	12.071160	3.608965	15.74483	0.044297	12.13587	cullin; ubiquitin ligase that targets Ddb1 (another MIG, below) and Ddb2, both of which act to initiate the DNA damage response, for ubiquitination and degradation, thereby regulating the DNA damage response (PMID: 19481525)
Dna2	*Dna2l*	3.9216094	3.7578457	4.807850	17.42876	0.015044	12.62091	due to 5' to 3' endonuclease activity, involved in resection extension in homologous recombination-mediated DNA double stranded break repair (PMID: 28718810)

Ddb1	XPE, DDBA, XAP1, XPCE	86.093717	88.333331	0.461818	2.706198	0.004385	2.244381	large subunit of DNA damage-binding complex, which functions in nucleotide excision repair (PMID: 16951172); loss of *Ddb1* in mouse brain results in accumulation of cell cycle regulators and increased genomic instability, ultimately causing apoptosis of proliferating neuronal progenitors (PMID: 17129780)
E2f1	Rbp3, Rbap1, Rbbp3	6.067779	6.486815	12.91249	53.23981	0.000964	40.32732	upregulated in response to DNA damage, and promotes DNA damage-induced apoptosis (PMID: 11459832); indirectly regulates the transcription of the DNA damage response gene *GADD45A* (PMID: 20713352)
Ercc5	Xpg	5.363914	6.275879	1.333767	7.642992	0.048076	6.309225	single strand-specific DNA endonuclease involved in the 3' incision step of nucleotide excision repair (PMID: 7657672)
Exo1	Msa, Hex1	4.4268470	4.1420745	3.731127	9.386061	0.008405	5.654934	5' to 3' endonuclease involved in DNA mismatch repair and resection extension in homologous recombination-mediated DNA double stranded break repair (PMID: 24705021)
Ints7		8.821004	8.814813	3.590800	13.52046	0.012655	9.929663	recruited to sites of DNA damage and interacts with SSB1, a DNA damage sensor recognized by ATM (PMID: 21659603)
Parp1	Parp, Ppol, Adprt, Artd1, Adprt1	47.879274	47.679811	0.771961	14.72329	0.002560	13.95133	nuclear protein that promotes formation of poly(ADP-ribose) chains (PARylation), which transfers ADP-ribose group from NAD+ to target protein and forms a scaffold around DNA breaks, allowing for recruitment of essential DNA damage response factors (PMID: 21989215, 22431722)
Usp10	UBPO, Uchrp	10.625277	8.050707	4.474797	17.26511	0.012563	12.79031	after DNA damage, phosphorylated by ATM, resulting in Usp10 stabilization and transport to the nucleus, where it deubiquitylates p53, thereby stabilizing p53 (PMID: 20096447)

Table S7. Primer sequences for RT-PCR.

Primer Name	Primer Direction	Sequence (5' to 3')
Rnu11 cKO, 5' loxP	Forward (primer 1)	ACCCTCCCCTACTGTTTTAC
	Reverse (primer 2)	AGGCTGCTACAGGATGACTC
Rnu11 cKO, 3' loxP	Forward (primer 3)	CATGTGTTTGCTGGGAATTG
	Reverse (primer 4)	CTCATGAGGCAGATCTCTGAA
Hist1h1a expression	Forward	AGAAGAACAACAGCCGCATCAAACTGG
	Reverse	CTTGGACTCAGCCTTCTTGTTCAGCTT
Cre genotyping	Forward	TATCCAGCAACATTTGGGCCAGCT
	Reverse	AACATTCTCCCACCGTCAGTACGTGA
Emx1-Cre zygosity, wild-type	Forward	AAGGTGTGGTTCCAGAATCG
	Reverse	CTCTCCACCAGAAGGCTGAG
Emx1-Cre zygosity, mutant	Forward	GATCTCCGGTATTGAAACTCCAGC
	Reverse	GCTAAACATGCTTCATCGTCGG
U11 expression	Forward	AAAGGGCTTCTGTCGTGAGTGGC
	Reverse	CCGGGACCAACGATCACCAG
Neat1 expression	Forward	AATTGGCCAGAAGACAACAGGGTTTGC
	Reverse	GTATTCAGTGGCAAAGCACTCATGAGG
Coa3 minor intron splicing	Forward	CAGTTGCAGTTTATGCGGCAGGTG
	Reverse (intronic)	CTAGCCACCCTTGCTGTTTTCCCAAA
	Reverse (exonic)	CAGCTTTGGCTTCATCTTCCAGCTC
Pten minor intron splicing	Forward	CTCCCAGACATGACAGCCATCATCAA
	Reverse (intronic)	CTACTCCCACGTTATCAGAGTGACAGAA
	Reverse (exonic)	CAAGTCTTTCTGCAGGAAATCCCATAGC
Parp1 minor intron splicing	Forward	AAAACCACCCCTGACCCTTCG
	Reverse (intronic)	GCACACAGCATAGCCAAGAAAGG
	Reverse (exonic)	AATGTACCTGGGGAGGGCAGTT
Sfrs10 expression	Forward	AGCAGGTCTTACAGCCGAGATTATCG
	Reverse	CCAAACACGCCAAGACAACAGTTG
Spc24 expression	Forward	CTCATACCTTGCACAGAACTGGGGTT
	Reverse	AATAAAAAGAAGCTGCAGGCCAGCC
Intergenic primers	Forward	GGATAGTTCATCTCCTGCAGGTCACAAG
	Reverse	GTCCCACCCATCTAGTTTAGCATCAGC

Table S8. Summary of statistical analyses performed.

Fig.	Experimental Paradigm (ex: immuno-staining)	*N*-value	*P*-value	t/f-value	Statistical test	Test for multiple testing?	Does data meet assumption of normality?
1B	qPCR	WT=3 WT/KO=3	6.43E-05	17.38388	Student's t-test [1]	No	Yes
1C	Genotype frequency	WT=20 Het=45 Mut=0	0.0001067	N/A	Chi-squared goodness of fit test	No	Yes
1J	Pallium thickness	Ctrl=3 Mut=3	0.63251 (E12) 0.96958 (E13) 0.02533 (E14)	-0.5168 (E12) 0.0405 (E13) 3.4805 (E14)	Student's t-test [1]	No	Yes

2A	TUNEL	Ctrl=3 Mut=3	0.587853	-0.58845	Student's t-test [1]	No	Yes
2B	TUNEL	Ctrl=4 Mut=4	0.000364	-7.19759	Student's t-test [1]	No	Yes
2C	TUNEL	Ctrl=3 Mut=3	0.001647	-7.55204	Student's t-test [1]	No	Yes
2D	TUNEL	Ctrl=4 Mut=4	0.017318	-3.25681	Student's t-test [1]	No	Yes
2E	CC3	Ctrl=3 Mut=3	0.348641	-1.06066	Student's t-test [1]	No	Yes
2F	CC3	Ctrl=4 Mut=4	0.006263	-4.11334	Student's t-test [1]	No	Yes
3D	Ki67	Ctrl=3 Mut=3	0.94384 (E12) 0.00114 (E13) 9.86E-05 (E14)	0.07497 (E12) 8.31546 (E13) 15.6004 (E14)	Student's t-test [1]	No	Yes
3D	NeuN	Ctrl=3 Mut=3	0.58591 (E12) 0.50374 (E13) 0.00256 (E14)	0.59165(E12) 0.73383 (E13) 6.71922 (E14)	Student's t-test [1]	No	Yes
3H	Pax6	Ctrl=3 Mut=3	0.91943 (E12) 0.00063 (E13) 2.83E-06 (E14)	0.1076 (E12) 9.6834 (E13) 38.116 (E14)	Student's t-test [1]	No	Yes
3L	Tbr2	Ctrl=3 Mut=3	0.983274 (E12) 0.030437 (E13) 0.001203 (E14)	-0.0223 (E12) 3.2822 (E13) 8.2035 (E14)	Student's t-test [1]	No	Yes
4B	qRT-PCR	Ctrl=4 Mut=4	0.000109	8.944523	Student's t-test [1]	No	Yes
4C	qRT-PCR	Ctrl=4 Mut=4	0.004161	4.487097	Student's t-test [1]	No	Yes
4E	yH2AX	Ctrl=3 Mut=3 (E11) Ctrl=3 Mut=4 (E12)	0.039021 (E11) 0.027471 (E12)	-3.02372 (E11) -4.02969 (E12)	Student's t-test [1] (E11) T-test: two sample assuming unequal variances (E12)	No	Yes
4E	P53	Ctrl=3 Mut=3 (E11) Ctrl=3 Mut=4 (E12)	0.57902 (E11) 0.01497 (E12)	0.60302 (E11) -5.05123 (E12)	Student's t-test [1] (E11) T-test: two sample assuming unequal variances (E12)	No	Yes
4G	Pax6/ p53	Mut=3	P<0.001 (Fisher's method) 0.1651 (N=1) 2.53E-04	N/A	Fisher Exact test[2]	No	Yes

			(N=2) 6.72E-04 (N=3)				
5C	Ki67/ PH3	Ctrl=5 Mut=5	0.036877	-2.50113	Student's t-test [1]	No	Yes
5D	Pax6/ AuroraB (M)	Ctrl=3 Mut=3	0.281507	-1.24374	Student's t-test [1]	No	Yes
5E	Pax6/ AuroraB	Ctrl=4 Mut=4	0.050205 (prophase) 0.022396 (prometaphase/ metaphase) 0.399731 (anaphase) 0.853745 (telophase)	2.443901 (prophase) -3.05402 (prometaphase/ metaphase) 0.906253 (anaphase) 0.19244 (telophase)	Student's t-test [1]	No	Yes
5F	Citk	Ctrl=3 Mut=3 (E11) Ctrl=4 Mut=4 (E12)	0.909922 (E11) 0.001502 (E12)	-0.1205 (E11) 5.5091 (E12)	Student's t-test [1]	No	Yes
5G	Pax6/ EdU	Ctrl=3 Mut=4	0.00013	10.58504	T-test: two sample assuming unequal variances	No	Yes
5H	Tbr2/ EdU	Ctrl=3 Mut=3	0.143103	1.972462	Student's t-test [1]	No	Yes
6A	yH2AX/ EdU	Mut=3	0.5<P<0.6 (Fisher's method) 0.0953 (n=1) 0.762 (n=2) 1.0 (n=3)	N/A	Fisher Exact test[2]	No	Yes
6B	P53/EdU	Mut=3	P<0.001 (Fisher's method) 0.0095 (N=1) 0.4087 (N=2) 4.61E-06 (N=3)	N/A	Fisher Exact test[2]	No	Yes
6C	P53/ AuroraB (M)	Mut=4	P<0.001 (Fisher's method) 3.94E-06 (N=1) 3.24E-04 (N=2) 0.0135 (N=3) 0.0115 (N=4)	N/A	Fisher Exact test[2]	No	Yes
6C	P53/ AuroraB (G2)	Mut=4	P<0.001 (Fisher's method) 9.18E-05	N/A	Fisher Exact test[2]	No	Yes

			(N=1) 2.76E-06 (N=2) 0.0321 (N=3) 2.01E-07 (N=4)				
6D	EdU/CC3	Mut=3	0.4<P<0.5 (Fisher's method) 0.345 (N=1) 0.586 (N=2) 0.265 (N=3)	N/A	Fisher Exact test[2]	No	Yes
S2C	CC3/pyknotic cells	Ctrl=3 Mut=3	0.001891	-7.28116	Student's t-test [1]	No	Yes
S2C	CC3/Tuj1	Ctrl=3 Mut=3	0.140357	-1.83533	Student's t-test [1]	No	Yes
S2D	Pax6	E12=3 E13=3 E14=3	0.001 (ANOVA) 0.002 (E12-E13) 0.719py (E13-E14)	30.835 (ANOVA)	One–way ANOVA	Post-hoc Tukey	Yes
S2E	Tbr2	E12=3 E13=3 E14=3	0.046 (ANOVA) 0.284 (E12-E13) 0.039 (E13-E14)	5.351 (ANOVA)	One–way ANOVA	Post-hoc Tukey	Yes
S2F	BrdU/ NeuN	Ctrl=3 Mut=3	0.0115 (%NeuN) 0.96281 (%BrdU)	4.416383 (%NeuN) 0.049606 (%BrdU)	Student's t-test [1]	No	Yes
S3A	qRT-PCR	Ctrl=3 Mut=3	0.009763 (Coa3) 0.014807 (Pten) 2.13E-06 (Parp1)	-4.6360 (Coa3) -4.1038 (Pten) -40.90389 (Parp1)	Student's t-test [1]	No	Yes
S4B	Tbr2/ AuroraB	Ctrl=4 Mut=4 (G2) Ctrl=3 Mut=3 (M)	0.544268 (G2) 0.890293 (M)	0.642447 (G2) -0.14693 (M)	Student's t-test [1]	No	Yes
S4C	Tbr2/ AuroraB	Ctrl=4 Mut=4	0.109109 (prophase) 0.640059 (prometaphase/ metaphase) 0.266296 (anaphase) 0.258209 (telophase)	-1.8803 (prophase) 0.492213 (prometaphase/ metaphase) 1.225527 (anaphase) 1.248928 (telophase)	Student's t-test [1]	No	Yes
S4E	Pax6/ EdU	Ctrl=3 Mut=3	0.114046	-2.01577	Student's t-test [1]	No	Yes
S4F	Cyclin B1	Ctrl=3	0.196738	1.547139	Student's	No	Yes

		Mut=3			t-test [1]		
S4G	Pax6/ AuroraB (G2)	Ctrl=3 Mut=3	0.223782	1.438129	Student's t-test [1]	No	Yes

[1] Two-sample t-test assuming equal variances

[2] Followed by Fisher's method to combine *P*-values